Extremely red quasars from SDSS, BOSS and WISE: classification of optical spectra

Monthly Notices
of the
ROYAL ASTRONOMICAL SOCIETY

MNRAS **453,** 3932–3952 (2015) doi:10.1093/mnras/stv1710

Extremely red quasars from SDSS, BOSS and *WISE*: classification of optical spectra

Nicholas P. Ross,[1,2★] Fred Hamann,[3] Nadia L. Zakamska,[4] Gordon T. Richards,[1,5] Carolin Villforth,[3,6] Michael A. Strauss,[7] Jenny E. Greene,[7†] Rachael Alexandroff,[4] W. Niel Brandt,[8,9] Guilin Liu,[4] Adam D. Myers,[5,10] Isabelle Pâris[11] and Donald P. Schneider[8,9]

[1]*Department of Physics, Drexel University, 3141 Chestnut Street, Philadelphia, PA 19104, USA*
[2]*Institute for Astronomy, SUPA[‡], University of Edinburgh, Royal Observatory, Edinburgh EH9 3HJ, UK*
[3]*Department of Astronomy, University of Florida, Gainesville, FL 32611-2055, USA*
[4]*Department of Physics and Astronomy, Johns Hopkins University, 3400 N. Charles St, Baltimore, MD 21218, USA*
[5]*Max-Planck-Institut für Astronomie, Königstuhl 17, D-69117 Heidelberg, Germany*
[6]*SUPA, School of Physics and Astronomy, University of St Andrews, North Haugh, St Andrews, Fife KY16 9SS, UK*
[7]*Department of Astrophysical Sciences, Princeton University, Princeton, NJ 08544, USA*
[8]*Department of Astronomy and Astrophysics, The Pennsylvania State University, University Park, PA 16802, USA*
[9]*Institute for Gravitation and the Cosmos, The Pennsylvania State University, University Park, PA 16802, USA*
[10]*Department of Physics and Astronomy, University of Wyoming, Laramie WY 82071, USA*
[11]*INAF – Osservatorio Astronomico di Trieste, Via G. B. Tiepolo 11, I-34131 Trieste, Italy*

Accepted 2015 July 24. Received 2015 July 24; in original form 2014 May 2

ABSTRACT

Quasars with extremely red infrared-to-optical colours are an interesting population that can test ideas about quasar evolution as well as orientation, obscuration and geometric effects in the so-called AGN unified model. To identify such a population, we match the quasar catalogues of the Sloan Digital Sky Survey (SDSS), the Baryon Oscillation Spectroscopic Survey (BOSS) to the *Wide-Field Infrared Survey Explorer* (*WISE*) to identify quasars with extremely high infrared-to-optical ratios. We identify 65 objects with $r_{\rm AB} - W4_{\rm Vega} > 14$ mag (i.e. $F_\nu(22\,\mu{\rm m})/F_\nu(r) \gtrsim 1000$). This sample spans a redshift range of $0.28 < z < 4.36$ and has a bimodal distribution, with peaks at $z \sim 0.8$ and $z \sim 2.5$. It includes three $z > 2.6$ objects that are detected in the *W*4 band but not *W*1 or *W*2 (i.e. '*W*1*W*2 dropouts'). The SDSS/BOSS spectra show that the majority of the objects are reddened type 1 quasars, type 2 quasars (both at low and high redshift) or objects with deep low-ionization broad absorption lines (BALs) that suppress the observed *r*-band flux. In addition, we identify a class of type 1 permitted broad emission-line objects at $z \simeq 2$–3 which are characterized by emission line rest-frame equivalent widths (REWs) of $\gtrsim$150 Å, much larger than those of typical quasars. In particular, 55 per cent (45 per cent) of the non-BAL type 1s with measurable C IV in our sample have REW(C IV) > 100 (150) Å, compared to only 5.8 per cent (1.3 per cent) for non-BAL quasars in BOSS. These objects often also have unusual line ratios, such as very high N V/Ly α ratios. These large REWs might be caused by suppressed continuum emission analogous to type 2 quasars; however, there is no obvious mechanism in standard unified models to suppress the continuum without also obscuring the broad emission lines.

Key words: surveys – galaxies: evolution – quasars: general – infrared: galaxies.

1 INTRODUCTION

Quasars are the most luminous non-transient objects in the Universe, with $L_{\rm bol}$ reaching $\sim 10^{47–48}$ erg s^{-1}, powered by accretion of matter on to supermassive black holes. To explain how quasars are fuelled and become active, models (e.g. Sanders et al. 1988; Hopkins et al. 2005, 2006) suggest that mergers between gas-rich galaxies produce starbursts and drive gas to the inner galactic nuclear regions. This activity fuels the growth of the supermassive black holes, which actively accrete matter at this stage, with much of the black hole growth happening in this ultraviolet (UV) and optically obscured

★ E-mail: npross@roe.ac.uk
† Alfred P. Sloan Fellow.
‡ Scottish Universities Physics Alliance.

phase. Feedback, potentially from a radiation-driven quasar wind, leads to removal of gas and dust from the central region, allowing the quasar to be seen in the UV and optical. These major-merger models are invoked to explain the obscuration/reddening observations noted in e.g. Urrutia, Lacy & Becker (2008), Glikman et al. (2012), and predict that red/obscured quasars should appear preferentially during an early stage of quasar evolution. However, the exact nature of the active galactic nucleus (AGN) triggering mechanism is not straightforward, as observations find that levels of disturbance in AGN hosts are consistent with those of inactive control samples (e.g. Kocevski et al. 2012; Villforth et al. 2014), or only slightly elevated at low-z (Rosario et al. 2015).

Quasars appear with a wide range of observational properties. Intrinsically luminous quasars may or may not appear bright at optical, UV and X-ray wavelengths. Much of this variance can be explained in the context of the geometry-based 'unification models' (Antonucci 1993). If gas and dust are present near the active nucleus but do not completely surround it, then some lines of sight to the nucleus are clear, whereas others are blocked. In the former case, the observer can directly view the emission from the accretion disc, with the quasar appearing bright at X-ray, UV and optical wavelengths; these objects are termed unobscured AGNs. Often these objects display broad (several thousand $\mathrm{km\,s^{-1}}$) emission lines in the optical spectra and are classified as 'type 1' quasars (Khachikian & Weedman 1974). Less-than-complete blockage of the quasar continuum by dust will redden the spectrum (e.g. Richards et al. 2003; Krawczyk et al. 2015).

This contrasts with the situation where the observer's line of sight is blocked by circumnuclear clouds; in this case, X-rays are absorbed by the intervening gas and UV and optical photons are scattered and absorbed by the intervening dust. At optical wavelengths, often the only signature of nuclear activity in this case is strong, narrow emission lines produced in the material illuminated by the quasar along unobscured directions. These objects with weak UV and optical continua are obscured AGNs, and if narrow UV/optical emission lines are present, are designated type 2 sources (Antonucci & Miller 1985; Smith et al. 2002; Zakamska et al. 2003; Brandt & Hasinger 2005; Reyes et al. 2008). Thus, obscuration, as part of an evolutionary phase or an orientation effect, is critical in determining the observed properties of quasars. However, because of their faintness at rest-frame optical and UV wavelengths, identifying obscured objects, at the peak of quasar activity $z \sim 2$, remains challenging (Norman et al. 2002; Stern et al. 2002; Alexandroff et al. 2013; Greene et al. 2014).

The circumnuclear clouds of gas and dust absorb X-ray, UV and optical radiation from the quasar and re-emit this energy thermally at infrared (IR) wavelengths. This is why unobscured quasars have similar luminosities at near- and mid-IR wavelengths ($\sim 2-30\,\mu\mathrm{m}$ in the rest frame) as they do in the optical and in the UV (Elvis et al. 1994; Richards et al. 2006; Polletta et al. 2008; Elvis 2010). Extremely obscured and dusty objects, in which optical emission is partially extinct or completely blocked, are therefore expected to show much higher IR-to-optical ratios than unobscured quasars. Indeed, a host of previous studies have used a K-band excess selection (Chiu et al. 2007; Jurek et al. 2008; Maddox et al. 2008, 2012; Nakos et al. 2009; Souchay et al. 2009; Wu & Jia 2010; Peth, Ross & Schneider 2011; Wu et al. 2011, 2013; Fynbo et al. 2013), a near-IR+radio selection (Glikman et al. 2004, 2007, 2012, 2013) or a mid-IR selection (Lacy et al. 2004; Stern et al. 2005, 2012; Martínez-Sansigre et al. 2006; Richards et al. 2009; Donley et al. 2012; Assef et al. 2013; Banerji et al. 2013) to identify obscured (as well as unobscured) AGN.

In this paper, we describe a search for quasars with extremely red colours in order to study their range of spectral properties. We use optical photometry and spectroscopy from the Sloan Digital Sky Survey (SDSS; York et al. 2000) and the SDSS-III (Eisenstein et al. 2011) Baryon Oscillation Spectroscopic Survey (BOSS; Dawson et al. 2013) as well as mid-IR photometry from the *Wide-Field Infrared Survey Explorer* (*WISE*; Wright et al. 2010). A companion paper (Hamann et al., in preparation) presents a detailed investigation into a new class of objects, the EREW quasars, which are introduced here.

This paper is organized as follows. In Section 2, we describe our data sets and sample selection, and in Section 3, we present the basis sample properties of the extremely red quasars. In Section 4, we discuss the optical spectra of the extremely red quasars, classifying objects along the traditional lines of broad-line type 1s, narrow-line type 2s and those with interesting absorption features. In Section 4.7, we introduce the new class of extreme EW quasars. In Section 5, we discuss the selection of the extremely red quasars and place these objects in a broader physical and evolutionary context. We conclude in Section 6.

2 DATA AND SAMPLE SELECTION

2.1 Parent data set

Our starting point is the spectroscopic quasar catalogues of the SDSS Seventh Data Release (DR7Q; Schneider et al. 2010; Shen et al. 2011) and the SDSS-III Tenth Data Release (DR10Q; Pâris et al. 2014). SDSS quasar targets with $i \leq 19.1$ were selected if the colours were consistent with being at redshift $z \lesssim 3$, and $i \leq 20.2$ objects were selected if $z \gtrsim 3$, as outlined in Richards et al. (2002). BOSS quasar targets are selected to a magnitude limit of $g \leq 22.0$ or $r \leq 21.85$, with the primary goal to select quasars in the redshift range $2.2 \leq z \leq 3.5$ as described by Ross et al. (2012, and references therein). In both SDSS and BOSS, quasar targets are also selected if they are matched within 2 arcsec (1 arcsec in the case of BOSS) of an object in the Faint Images of the Radio Sky at Twenty-cm (FIRST) catalogue of radio sources (Becker, White & Helfand 1995). Both the SDSS DR7Q and BOSS DR10Q include quasars that were selected by algorithms other than the main quasar selections; these sources appear in the catalogue due to being targeted by the respective galaxy selections, being a 'serendipitous' (Stoughton et al. 2002) or 'special' (Adelman-McCarthy et al. 2006) target in SDSS, or an 'ancillary' target in BOSS (Dawson et al. 2013; Alam et al. 2015).

Luminous distant quasars are expected to be unresolved in optical ground-based observations, so we use point spread function (PSF) magnitudes reported in the SDSS DR7 and BOSS DR10 quasar catalogues, corrected for Galactic extinction (Schlegel, Finkbeiner & Davis 1998). Using the 2.5 m Sloan telescope (Gunn et al. 2006), imaging data (Gunn et al. 1998) and spectra were obtained with the double-armed SDSS/BOSS spectrographs which have $R = \lambda/\mathrm{FWHM} \sim 2000$ (Smee et al. 2013). Redshifts are measured from the spectra using the methods described in Bolton et al. (2012) and the data products are detailed in the SDSS DR7 (Abazajian et al. 2009) and DR10 (Ahn et al. 2014) papers.

The SDSS DR7 and BOSS DR10 quasar catalogues include 105 783 objects across 9380 $\mathrm{deg^2}$, and 166 583 objects across 6370 $\mathrm{deg^2}$, respectively, with 16 420 objects in common to both catalogues. Thus, our superset of optical data has 255 946 objects, and we use the BOSS spectrum (which has higher SNR and a larger

Table 1. Overview of the numbers of SDSS/BOSS quasars in the *WISE*-matched data set. The third row gives the number of quasars which satisfy $W4$ SNR $\geq$3; the fourth row is the number of quasars having a magnitude of $W4 - \sigma_{W4} \leq 8.00$, while the fifth row is the number having $W4 \leq 8.00$. Numbers of objects passing the $r_{\rm AB} - W4_{\rm Vega}$ colour cut is given.

Description	Unique objects	from SDSS	from BOSS
DR7Q and DR10Q quasars[a]	255 946	105 783	166 583
‖ + matched to *WISE*	203 680	102 083	111 779
‖ + $\rm SNR_{W4} \geq 3$	52 873	41 922	10 951
‖ + $W4 - \sigma_{W4} \leq 8.00$	28 513	24 041	4 472
‖ + $W4 \leq 8.00$	18 615	16 035	2 580
‖ + `cc_flags`	[b]17 744	15 300	2 444
and $r - W4 > 13.0$	286	104	182
and $r - W4 > 13.5$	136	34	102
and $r - W4 > 14.0$	**65**	**19**	**48**

[a]There are objects common to both SDSS DR7Q and BOSS DR10Q that have *WISE* matches. Hence, the sum of the 'From SDSS' and 'From BOSS' columns is greater than the given total.
[b]'Good' $W4$ detections have $\rm SNR_{W4} \geq 3$ and $W4 < 8.00$ and `cc_flags` equal to '0000'.

wavelength coverage) when there are duplicate spectra between the two catalogues.

WISE mapped the sky in four filters centred at 3.4, 4.6, 12 and 22 μm ($W1$, $W2$, $W3$ and $W4$ bands), achieving 5σ point-source sensitivities better than 0.08, 0.11, 1 and 6 mJy, respectively. The *WISE* Explanatory Supplement[1] provides further details about the astrometry and photometry in the source catalogue. We retrieved photometric quantities for each of the four *WISE* bands. Hereafter, we use the notation $\rm SNR_{Wx}$ for the signal-to-noise ratio and Wx for the Vega-based *WISE* magnitudes, in band $x = 1, 2, 3$ and 4.

Because of established conventions, we report SDSS *ugriz* magnitudes on the AB zero-point system (Oke & Gunn 1983; Fukugita et al. 1996), while the *WISE* $W1 - 4$ magnitudes are calibrated on the Vega system (Wright et al. 2010). For *WISE* bands, $m_{\rm AB} = m_{\rm Vega} + \Delta m$ where $\Delta m = (2.699, 3.339, 5.174, 6.620)$ for $W1$, $W2$, $W3$ and $W4$, respectively (Cutri et al. 2011). We make use of the Explanatory Supplement to the *WISE* All-Sky Data Release, as well as the *WISE* AllWISE Data Release Products online.

The *WISE* team has released two all sky catalogues: the nine-month cryogenic phase of the mission led to the *WISE* All-Sky ('AllSky') Data Release; while the *WISE* AllWISE Data Release ('AllWISE') combines the AllSky data with the NEOWISE programme (Mainzer et al. 2011). The resulting AllWISE data set is deeper in the two shorter *WISE* bands (5σ point-source sensitivities now 0.054 and 0.071 mJy), and the data processing algorithms were improved in all four W bands. Our analysis began with AllSky, moved to ALLWISE when it became available, but we use both since we had already performed visual inspections using AllSky.

We match the sample of the 255 946 unique quasars in the SDSS DR7Q and BOSS DR10Q, and use both the AllSky and the AllWISE data available at the NASA/IPAC Infrared Science Archive (IRSA),[2] with a matching radius of 2 arcsec. For the combined DR7Q+DR10Q, we find 203 680 matches; 102 083 objects (96.5 per cent) of the DR7Q and 111 779 (67 per cent) of the DR10Q are matched in one or more *WISE* bands. The difference in the percentage of matches is expected since BOSS is fainter than SDSS. Matching with DR10Q positions offset in right ascension and declination by 6, 12 and 18 arcsec (∼1, 2 and 3 times the *WISE* angular resolution in $W1/2/3$) return, respectively, 508, 893 and 873 matches within 2 arcsec, suggesting our false-positive matching rate is $\lesssim$1 per cent (see also Krawczyk et al. 2013).

With a matching radius of 2 arcsec, 15 843 of the SDSS DR7 quasars, and 2 979 of the (optically fainter) BOSS DR10 quasars have a good match in the *WISE* $W4$ band, i.e. $\rm SNR_{W4} \geq 3$, $W4$<8.00 (close to the nominal 5σ point source sensitivity of $W4 = 7.9$ mag; Wright et al. 2010) and the *WISE* contamination and confusion flag, `cc_flags` set to '0000', suggesting the source is unaffected by known artefacts in all four bands. Table 1 presents an overview of the numbers of SDSS/BOSS quasars in the *WISE*-matched data set.

2.2 Extremely red quasar criterion

Dey et al. (2008) discovered a population of $z \sim 2$ dust-obscured galaxies, revealed by the *Spitzer Space Telescope*. In addition to having AGN activity, these objects are strongly star forming and dusty which contributes to their red colours (Brand et al. 2008; Pope et al. 2008; Soifer, Helou & Werner 2008; Bussmann et al. 2009a,b; Melbourne et al. 2009, 2012). Motivated by this finding, we apply similar selection criteria to the SDSS/BOSS+*WISE* matched quasars; see Fig. 1. At high redshift our *WISE* $W4$ i.e. 22 μm-based selection, is sensitive to hot dust since $W4$ probes $\lambda \simeq 7.3$ μm at $z \approx 2$ (Draine & Li 2007; Elitzur 2008; Diamond-Stanic & Rieke 2010). This is of particular interest because at these redshifts shorter wavebands (e.g. $W1$) may cease to trace dust emission, i.e. $W1$ probes $\lambda \simeq 1$ μm, where dust does not emit strongly.

In particular, we require the spectroscopic quasars to have a reliable detection in the *WISE* $W4$ band:

$$\rm SNR_{\it W4} \geq 3, \quad (1)$$

a colour of

$$r_{\rm AB} - W4_{\rm Vega} > 14.0 \quad (2)$$

i.e. $r_{\rm AB} - W4_{\rm AB} \gtrsim 7.5$, which corresponds to $F_\nu(22\,\mu{\rm m})/F_\nu(r) \gtrsim 1000$, and

$$W4_{\rm Vega} \leq 8.00. \quad (3)$$

We further include objects with $W4 > 8.00$ if the object has $\rm SNR_{W4} \geq 3$ and $W4$–$\sigma_{W4} < 8.00$. In Table 1, we outline the stages in the selection and the resulting number of quasars after every step.

[1] wise2.ipac.caltech.edu/docs/release/allwise/expsup/index.html
[2] http://irsa.ipac.caltech.edu/

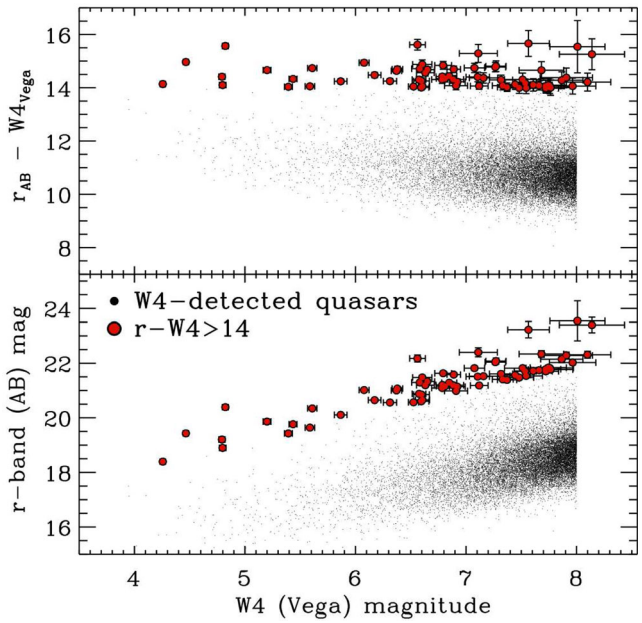

Figure 1. Top: $r - W4$ colour of the $W4$-detected SDSS/BOSS quasars (black dots) as a function of $W4$ (i.e. 22 μm) magnitude. The quasars with $r - W4 > 14$ are shown as large red circles. Bottom: the $r_{\rm AB}$-band magnitude versus $W4$. As a guide, $W4_{\rm Vega} = 8.0$ mag corresponds to $W4_{\rm AB} = 14.6$, or a flux density of $F_\nu \approx 6$ mJy (Wright et al. 2010).

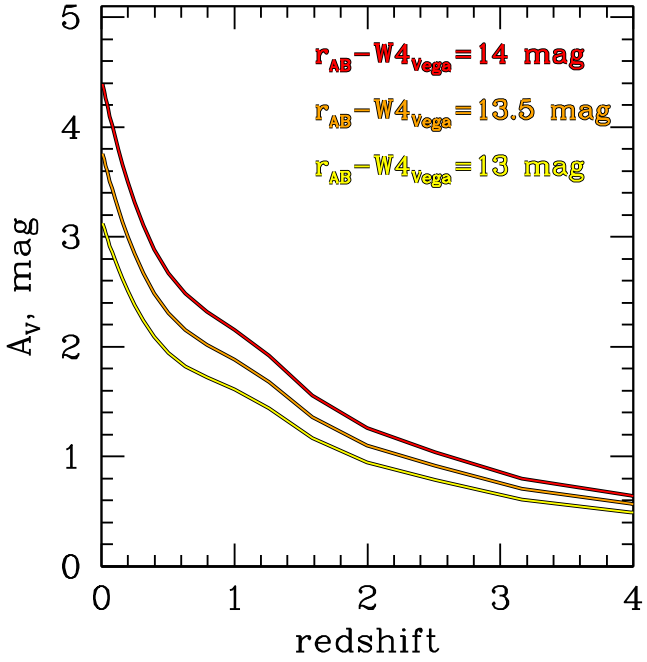

Figure 2. The minimal amount of dust extinction required to produce high IR-to-optical ratios consistent with our selection criteria, as a function of the redshift of the quasar. The Richards et al. (2006) SED for bright quasars is assumed to represent an unextinct mean quasar. We then apply varying amounts of SMC-like extinction (from Weingartner & Draine 2001) and convolve with the respective filter curves. We assume $R_V \equiv \frac{A_V}{E(B-V)} = 2.87$ (Gordon & Clayton 1998). The three curves show the A_V values required to generate colours of $r - W4 > 13$ (yellow) $r - W4 > 13.5$ (orange) and $r - W4 > 14$ (red).

The $r - W4 > 14$ selection has been shown to select type 2 quasars with $z \sim 2$ (Brand et al. 2006, 2007) and while both Dey et al. (2008) and our selection have a colour cut of $r_{\rm AB}$–$W4_{\rm Vega} > 14.0$, we note that Dey et al. (2008) went to much fainter magnitudes, basing their initial selection in the IR, matched to optical catalogues, and then obtained additional spectra of their candidates. Also, while Dey et al. (2008) start from the IR selection, we start with UV/visible selected quasars in SDSS/BOSS and then look at $W4$ to find the reddest cases.

Our selection applied to both the AllSky and AllWISE catalogues results in very similar samples, and any object that passes the criteria in equations (1)–(3) in either of these data releases is included. There are 65 quasars that have spectra from SDSS/BOSS and satisfy the extremely red criterion from the union between the two *WISE* data sets.

The $W4$ PSF has a full width at half-maximum (FWHM) of 12 arcsec, much larger than the optical PSF, so a nearby galaxy and a quasar cannot be deblended in $W4$ observations if they are only a few arcsec apart. To check this possibility, we visually inspected the SDSS and *WISE* images of the 65 objects using the SDSS Image List Tool and the IRSA *WISE* Image Service, and found that there is no other obvious optical source (down to the 5σ depth of the SDSS photometric survey of $r = 22.7$) within 6 arcsec of any of our targets. In only two cases, there is potential concern that another optical object boosts the $W4$ flux – we return to this in Section 4.4. We do note, however, that dusty star-forming galaxies (particularly at high redshift) are very faint optically, so there is still a possibility that there is an additional contaminating galaxy; inspecting the relatively shallow SDSS images only eliminates the possibility of optically bright contaminating galaxies.

Also, although they are bright in $W1$ and $W2$, brown dwarfs tend to be significantly fainter than eighth magnitude in $W4$ (Kirkpatrick et al. 2011); so, we do not suspect contamination from these objects. Thus we consider all 65 $r - W4 > 14$ quasars to be good matches.

2.3 Effects of dust extinction

Before we discuss in detail the observed spectral properties of our sample of extremely red quasars, we describe our expectations for how much extinction would be required to redden the overall spectral energy distribution (SED) of a quasar in order for it to be picked up by our colour selection. We acknowledge that the extremely red colours of our objects may not be all due to dust, and thus this exercise is for general guidance.

We simulate the colours of reddened quasars at different redshifts using the Richards et al. (2006) SED of bright quasars, assuming that the SEDs of all unextinct quasars are the same. We then apply varying amounts of SMC-like extinction (parametrized by the amount of extinction in the V band, A_V, in magnitudes), place this object at different redshifts and record its $r - W4$ colour.

The result is shown in Fig. 2, where the amount of extinction as a function of redshift is shown to generate colours of $r - W4 > 13$, $r - W4 > 13.5$ and $r - W4 > 14$ (the yellow, orange and red curves, respectively). The amount of extinction is very sensitive to the redshift of the quasar, and here we are only concerned with the dust reddening of a type 1 SED. If there is any optical emission that is not affected by the circumnuclear dust extinction – for example, the extended emission from the host galaxy – then it would make a reddened quasar appear less red in the $r - W4$ colour. Thus, the values of A_V plotted in Fig. 2 should be regarded as *lower* limits on the amount of quasar extinction to produce the requisite colours. At low redshifts, the observed r band probes rest-frame optical emission of the quasar; so, the amount of extinction necessary to produce a very red optical-to-IR colour is considerable. However, at high redshifts (where BOSS observations probe the rest-frame UV

emission), an A_V of just a few tenths is sufficient to strongly suppress the UV emission while having a small effect on the IR; this produces a very red $r - W4$ colour. Vardanyan, Weedman & Sargsyan (2014) discuss the rest 0.25 μm/7.8 μm luminosities and properties of $1.4 < z < 5$ quasars in the SDSS, and define 'obscured' quasars based on $\gtrsim$5 mag of UV extinction; considerably larger than we consider for our extremely red quasars over the same redshift range.

Due to the shallow nature of the *WISE W*4 band, at high redshift, any *W*4-detected galaxy that does not show nuclear activity will have $L_{IR} > 10^{12}$ $L_\odot$ and star formation rates $>100\,M_\odot$ yr^{-1}. Indeed, many of the non-AGN *WISE W*4 detections will have substantially higher IR luminosities and SFRs.

We have also checked the $R - W4$ colours of galaxies from the Canada–France–Hawaii Telescope Legacy Survey[3] and find that they again have a range of colours, $\sim 9 < R - W4 \lesssim 15$.

The optical colours of our sample are inconsistent with simple dust extinction of a standard quasar SED (e.g. Richards et al. 2003; Krawczyk et al. 2015) and this is a current area of investigation. We discuss possible solutions to this in our companion papers, Hamann et al. (in preparation) and Zakamska et al. (in preparation); in particular, contribution from scattered light is a possibility (e.g. Zakamska et al. 2005, 2006) and so is patchy obscuration Veilleux et al. (2013). In particular, we investigate further the nature of the obscuration from the SEDs, which is not consistent with simple reddening from our analysis. As such, we are very hesitant to draw any further conclusions on dust reddening and A_V values in this paper, and leave detailed discussions to Hamann et al. (in preparation).

3 KEY PROPERTIES OF THE EXTREMELY RED QUASARS

3.1 Magnitudes and redshift distribution

The key properties of the extremely red quasar sample are provided in Table 2: the catalogue name of the object, its right ascension, declination, redshift and magnitude and colour properties. The radio fluxes are the integrated flux densities (F_{int}) measured in mJy at 20 cm from the FIRST survey (Becker et al. 1995). The REWs are given for Mg II at $z \leq 1.5$ and C IV for objects at redshift $z > 1.5$. The FWHM of the relevant emission line is also quoted, with the REW and FWHM measurements coming from fits to the line profiles, as described in Hamann et al. (in preparation).

We give each object a classification based on optical spectral properties, indicated by the bitwise values described in Table 3. These classifications were all performed by visual inspection, with objects assigned to the classes given in Table 3 depending on the presence (or absence) of broad/narrow emission lines, broad absorption features, indications of ongoing or recently ceased star formation, or objects with large EW in the C IV emission line. These visual inspections are generally qualitative but as discussed in Section 4, aid us to understand the sample and physical types of quasars that the $r - W4 > 14$ colour selects. We also present a short note on each object in Table 2, qualitative assessments based on visual inspection of the optical spectra, and use these notes to make the link between the classifications given in Table 3 and the discussions presented in Section 4. We call a quasar 'red' when its spectral slope is shallower than the Vanden Berk et al. (2001) template. The acronym EREW stands for extreme rest-frame equivalent width, referring to a group of objects we introduce and describe in Section 4.7.

[3] http://www.cfht.hawaii.edu/Science/CFHLS/

The redshift range for the extremely red quasars is $0.282 < z < 4.36$, and half the sample is fainter than $r = 21.4$. Fig. 3 shows the redshift distribution of the sample compared to the full redshift distribution of the 17 744 SDSS/BOSS quasars with good *W*4 matches. The redshift distribution of the $r - W4 > 14$ sample is bimodal, with peaks around $z \sim 0.8$ and $z \sim 2.5$. This bimodality is the result of the two different SDSS quasar selections. The $z \sim 2.5$ redshift peak is due to the increased depth of the BOSS selection, as seen in Fig. 4.

In the left-hand panel of Fig. 4 the redshifts and *i*-band magnitudes are displayed for the $r - W4 > 14$ objects, and compared to the distributions from the full SDSS DR7 and BOSS DR10 quasar catalogues. SDSS quasars use the *i* band for selection limits; thus, one can identify the $i = 19.1$ magnitude limit contour for the SDSS $z \lesssim 2.5$ quasars, as well as the redshift histogram peaks at $z \sim 0.6$–1.0 and $z \sim 2.2$–2.7 seen in the BOSS quasar distribution (e.g. fig. 2 in Pâris et al. 2014). In the right-hand panel of Fig. 4, the extremely red quasars are compared to the SDSS/BOSS+*WISE* catalogue, for the fully matched (i.e. any *WISE* band) sample given by the black contours, and for the *W*4-matched objects only, given by the orange contours. The redshift *i* magnitude distribution of the ≈18 000 objects with good *W*4 matches is given by the orange contours and points. These *W*4 objects are at the bright end in the optical, and are generally at $z < 2$. Since we are selecting such extreme objects it is important to see how the selection affects the redshift distribution. In Fig. 5, we show how the number of objects selected, and the sample redshift, depend on $r - W4$ colour. The dip in mean redshift at $r - W4 \sim 10$–11 comes from the fact that fainter BOSS quasars, generally at $z \gtrsim 2$, are lost quicker than $z \lesssim 1$ quasars. The upturn at $r - W4 > 11.5$ is due to the fact that the *W*4-bright BOSS quasars that are very red remain in the sample even to the reddest colours.

Fig. 6 presents the magnitude–redshift and colour–redshift relations for the SDSS/BOSS+*WISE* matched catalogue highlighting the extremely red sample. This plot can be directly compared with Yan et al. (2013, and their fig. 20). Yan et al. (2013) have also merged the *WISE* photometry with the SDSS (though not BOSS), and describe the spectroscopic observations of eight objects that have $r - W4 > 14$ (see their Table 1 for details). Although we have an order of magnitude more $r - W4 > 14$ objects at $z > 2$, the Yan et al. objects are significantly fainter in the optical than our SDSS/BOSS detected objects. Based on the spectral properties of the Yan et al. (2013) sample, three (out of eight) objects are classified as type 1 AGN, three objects are type 2 AGN and the remaining two objects have features consistent with either a type 2 AGN, or a star-forming galaxy, broadly in line with the composition given in Table 3. Interestingly, Yan et al. (2013) motivate the use of the $r - W4 > 14$ colour selection in order to select ultraluminous infrared galaxy (ULIRG) candidates, not red quasars (they use the shorter *WISE* bands to select reddened quasars), and indeed find this colour selection identifies IR luminous galaxies over a wide range of redshift, $z \sim 0.7$–3. However, the relative contribution to the *W*4 luminosity from AGN and star formation warrants investigation, especially at high redshift where the rest-frame 22 μm can probe warm (AGN) dust, as well as polyaromatic hydrocarbon (PAH) features.

3.2 Mid-IR colours of the ERQs

The mid-IR colour–colour distributions for the SDSS/BOSS quasars that are detected in *WISE* are shown in Fig. 7. Contours are given for the full 'good' *W*4 sample, with objects that have redshifts $2 < z$ given by the blue and $z > 2$ given by red contours, respectively. The colours of the extremely red quasar sample are given by the large

Table 2. The 65 quasars from SDSS and BOSS that have $r - W4 > 14$, in order of increasing redshift. The *r*-band AB magnitude is from either Schneider et al. (2010) or Pâris et al. (2014), corrected for Galactic extinction (Schlegel et al. 1998), while the *WISE W*4 Vega magnitude is from the AllWISE Data Release catalogue. The radio fluxes are the integrated flux densities ($F_{\rm int}$) measured in mJy at 20 cm from the FIRST survey (Becker et al. 1995). The REWs in Åare given for Mg II at $z \leq 1.5$ and C IV for objects at redshift $z > 1.5$. The FWHM of the relevant emission line is also quoted. Objects with similar optical spectral properties are grouped together, using the bitwise values described in Table 3, converted here to binary (with a space gap for easier inspection).

Name (SDSS J)	RA (J2000)	Dec. (J2000)	z	r mag (AB)	$W4$ mag (Vega)	$r - W4$	Radio (flux/mJy)	REWs (Å)	FWHM (km s^{-1})	Notes	Spectral classification
101034.27+372514.7	152.642 83	37.420 77	0.282	18.39 ± 0.03	4.26 ± 0.02	14.14	–	–	–	Type 1; Strong narrow [O II], starburst	0000 0101
0941000.8+143614.4	145.253 39	14.604 02	0.384	19.43 ± 0.02	5.39 ± 0.04	14.04	7.6	–	–	Type 1; strong narrow [O II], starburst	0001 0110
105327.92+375804.2	163.366 36	37.967 86	0.448	19.64 ± 0.03	5.59 ± 0.04	14.05	2.8	–	–	Type 1; weak [O II], strong [Ne III] and [O III], post-starburst	0001 1010
112657.76+163912.0	171.740 69	16.653 34	0.464	19.20 ± 0.02	4.79 ± 0.03	14.41	2.4	–	–	Type 1; strong narrow [O III], post-starburst	0001 1010
102834.03−023659.6	157.141 82	−2.616 57	0.470	18.90 ± 0.02	4.80 ± 0.03	14.10	68.5	–	–	Type 1 based on Mg II, blazar candidate	0001 0001
110550.54+112702.0	166.460 59	11.450 58	0.498	20.65 ± 0.05	6.17 ± 0.06	14.48	2.9	–	–	Potential type 2 candidate, but broad H α	0001 0010
092501.78+274607.9	141.257 44	27.768 88	0.531	19.43 ± 0.02	4.47 ± 0.02	14.97	26.7	–	–	Type 2 in Reyes et al. (2008)	0001 0010
091157.55+014327.5	137.989 80	1.724 32	0.603	21.48 ± 0.08	6.60 ± 0.09	14.88	4.6	–	–	Type 2 in Reyes et al. (2008)	0001 0010
225612.16−010508.0	344.050 71	−1.085 56	0.651	21.53 ± 0.07	7.16 ± 0.13	14.37	3.0	27 ± 8	1870 ± 730	Type 2 in Reyes et al. (2008)	0001 0010
161558.92+252736.1	243.995 52	25.460 04	0.676	22.04 ± 0.09	7.26 ± 0.09	14.78	4.2	69 ± 8	918 ± 174	Type 2	0001 0010
111354.66+124439.0	168.477 76	12.744 18	0.680	19.86 ± 0.03	5.20 ± 0.04	14.66	4.2	–	–	Red type 1 (broad H β, strong [O II], Fe II)	0001 0101
124836.10+424259.3	192.150 43	42.716 50	0.682	21.61 ± 0.07	7.32 ± 0.10	14.29	3.4	22 ± 11	3103 ± 1138	Type 2	0001 0010
101303.09+072731.9	153.262 88	7.458 87	0.697	20.99 ± 0.05	6.91 ± 0.10	14.08	–	35 ± 5	1793 ± 294	Type 2	0000 0010
154215.25+161648.9	235.563 54	16.280 28	0.714	21.70 ± 0.06	7.54 ± 0.10	14.17	1.5	23 ± 6	1972 ± 507	Type 2	0001 0010
144642.28+011303.0	221.676 18	1.217 51	0.726	21.02 ± 0.05	6.08 ± 0.05	14.94	5.8	–	–	Type 2 in Reyes et al. (2008)	0001 0010
005009.81−003900.6	12.540 91	−0.650 17	0.728	20.11 ± 0.03	5.87 ± 0.06	14.24	4.4	–	–	Type 2	0001 0010
142240.99+383710.4	215.670 83	38.619 57	0.758	20.57 ± 0.03	6.53 ± 0.05	14.04	9.8	–	–	Type 2 in Reyes et al. (2008)	0001 0010
140744.00+360109.5	211.933 33	36.019 31	0.783	21.29 ± 0.05	6.85 ± 0.07	14.44	5.3	112 ± 5	(4000)	Type 1 with O II	0001 0101
124231.04+023307.0	190.629 33	2.551 95	0.785	21.16 ± 0.05	6.81 ± 0.08	14.35	–	–	–	Red type 1	0000 0001
091501.71+241812.1	138.757 14	24.303 36	0.844	20.39 ± 0.03	4.82 ± 0.03	15.57	10.1	–	–	Type 1; very bright in *W*4	0001 0001
152504.74+123401.7	231.269 77	12.567 15	0.851	21.14 ± 0.04	6.92 ± 0.07	14.22	–	43 ± 3	1984 ± 167	Type 2	0000 0010
151354.48+145125.2	228.477 02	14.857 02	0.881	21.00 ± 0.04	6.37 ± 0.05	14.63	7.6	20 ± 2	2212 ± 209	Type 2	0001 0010
144855.23+213622.0	222.230 16	21.606 12	0.882	21.70 ± 0.07	7.72 ± 0.12	13.98	5.2	101 ± 17	7868 ± 1347	Type 2	0001 0010
210712.77+005439.4	316.803 22	0.910 96	0.924	20.56 ± 0.03	6.31 ± 0.06	14.25	0.5	–	–	Type 1, strong Fe II, LoBAL Mg II absorption	0011 0001
075257.36+351834.6	118.239 01	35.309 62	0.926	23.23 ± 0.30	7.57 ± 0.19	15.66	–	52 ± 4	2979 ± 198	Type 1	0000 0001
141702.32+364839.5	214.259 69	36.810 98	1.004	21.58 ± 0.06	6.89 ± 0.06	14.69	7.8	181 ± 33	21698 ± 3680	Type 2	0001 0010
142131.51+210719.4	215.381 31	21.122 07	1.061	21.78 ± 0.08	7.72 ± 0.14	14.06	1.0	37 ± 4	1425 ± 137	Type 2	0001 0010
092356.70+230030.9	140.986 27	23.008 60	1.095	22.34 ± 0.12	7.68 ± 0.20	14.66	–	30 ± 8	2112 ± 410	Type 2, strong O II	0000 0110
091103.50+444630.3	137.764 58	44.775 11	1.302	20.88 ± 0.06	6.58 ± 0.06	14.30	–	–	–	Type 1; Strong Fe II emission, LoBAL Mg II absorption	0010 0001
111004.78+375236.7	167.519 94	37.876 86	1.308	20.34 ± 0.04	5.61 ± 0.04	14.74	7.1	–	–	Red type 1	0001 0001

Table 2 – *continued*

Name (SDSS J)	RA (J2000)	Dec. (J2000)	z	r mag (AB)	$W4$ mag (Vega)	$r-W4$	Radio (flux/mJy)	REWs (Å)	FWHM (km s^{-1})	Notes	Spectral classification
165258.51+390249.7	253.243 80	39.047 16	1.308	21.21 ± 0.04	6.79 ± 0.06	14.42	249.3	7 ± 1	2966 ± 304	Type 1 based on Mg II, blazar candidate	0001 0001
102425.41+033239.8	156.105 89	3.544 41	1.477	22.40 ± 0.17	7.11 ± 0.17	15.29	–	35 ± 8	1166 ± 377	Type 2 based on v. narrow C IV	0000 0010
144929.61+394824.2	222.373 41	39.806 74	1.491	21.74 ± 0.06	7.66 ± 0.11	14.08	24.3	57 ± 9	10075 ± 1405	Type 2 based on v. narrow C IV and He II	0001 0010
153542.41+090341.1	233.926 71	9.061 43	1.533	21.33 ± 0.04	6.65 ± 0.07	14.68	8.1	137 ± 14	1556 ± 140	Type 1; very strong Fe II emission in UV2/3, UV1, and strong Al III with weak/absent C III] and Si III]; see Appendix A1.	0011 0001
080304.76+532627.0	120.769 87	53.440 84	1.573	20.85 ± 0.05	6.60 ± 0.07	14.26	2.9	123 ± 7	3196 ± 138	Type 1; LoBAL	0011 0001
122453.20+084303.2	186.221 67	8.717 57	1.960	23.55 ± 0.73	8.01 ± 0.25	15.54	–	0 ± 0	0 ± 0	Red type 1	0000 0001
211329.61+001841.7	318.373 40	0.311 61	1.996	23.40 ± 0.28	8.14 ± 0.29	15.26	–	192 ± 7	1536 ± 49	Type 2, 'extreme' REW (EREW)	1000 0010
163313.29+401338.9	248.305 41	40.227 49	2.010	21.18 ± 0.05	7.12 ± 0.08	14.07	10.5	20 ± 10	11936 ± 99	Type 1; blazar candidate	0001 0001
173049.10+585059.5	262.704 59	58.849 88	2.035	21.39 ± 0.07	7.37 ± 0.09	14.02	–	–	–	Type 1; FeLoBAL	0010 0001
133611.79+404522.9	204.049 13	40.756 37	2.071	21.07 ± 0.06	6.38 ± 0.05	14.69	3.1	20 ± 3	6244 ± 688	Type 1	0001 0001
013435.66−093102.9	23.648 61	−9.517 48	2.220	21.30 ± 0.06	6.58 ± 0.07	14.71	960	–	–	Gravitational lens, red type 1, see Appendix A2	0001 0001
084447.66+462338.7	131.198 62	46.394 11	2.224	21.48 ± 0.08	7.48 ± 0.13	14.00	–	175 ± 4	1744 ± 34	Type 2, with narrow C IV	0000 0010
094317.59+541705.1	145.823 33	54.284 75	2.230	21.41 ± 0.07	7.33 ± 0.09	14.08	2.2	–	–	Type 1; FeLoBAL	0011 0001
222646.53+005211.2	336.693 90	0.869 80	2.247	21.54 ± 0.07	7.54 ± 0.15	14.00	653	65 ± 4	2663 ± 212	Red Type 1, strong associated absorbtion	0001 0001
000610.67+121501.2	1.544 49	12.250 35	2.309	22.18 ± 0.13	6.56 ± 0.07	15.61	–	108 ± 6	4589 ± 202	Type 1, EREW	1000 0001
232326.17−010033.1	350.859 06	−1.009 20	2.355	21.83 ± 0.08	7.76 ± 0.22	14.07	–	256 ± 5	3977 ± 62	Type 1, N v/Ly $\alpha > 1$, EREW	1000 0001
123241.73+091209.3	188.173 91	9.202 61	2.385	21.09 ± 0.05	6.78 ± 0.09	14.31	–	230 ± 3	4873 ± 53	Type 1, N v/Ly $\alpha > 1$, EREW	1000 0001
083413.90+511214.6	128.557 93	51.204 07	2.391	19.77 ± 0.04	5.43 ± 0.04	14.33	1.9	–	–	Type 1, red slope, z from absorption at red end	0001 0001
0832000.2+1615000.3	128.000 85	16.250 11	2.423	21.82 ± 0.08	7.51 ± 0.16	14.31	1.1	–	–	Type 1, EREW, strong associated absorption lines	1001 0001
011110.83+204543.8	17.795 17	20.762 18	2.432	22.03 ± 0.09	7.96 ± 0.21	14.06	–	0 ± 0	0 ± 0	Type 1; Ly α emitter QSO	0000 0001
090630.73+082837.3	136.628 06	8.477 05	2.437	21.77 ± 0.09	7.76 ± 0.20	14.00	22.8	3 ± 1	340 ± 159	Type 1 (from Ly α width)	0001 0001
093638.41+101930.3	144.160 06	10.325 10	2.458	21.72 ± 0.06	7.61 ± 0.17	14.11	–	169 ± 4	1273 ± 20	Type 2, but with EREW	1000 0010
134026.99+083427.2	205.112 48	8.574 24	2.490	22.31 ± 0.13	8.10 ± 0.21	14.21	–	338 ± 11	2088 ± 51	Type 2, but with EREW	1000 0010
221524.00−005643.8	333.850 03	−0.945 50	2.493	22.29 ± 0.12	7.91 ± 0.24	14.38	–	152 ± 5	4226 ± 112	Type 1; EREW	1000 0001
111017.13+193012.5	167.571 39	19.503 47	2.497	20.61 ± 0.03	6.59 ± 0.07	14.01	–	–	–	Type 1; EREW	1000 0010
155102.79+084401.1	237.761 63	8.733 66	2.520	20.66 ± 0.03	6.61 ± 0.06	14.05	2.9	10 ± 3	2467 ± 426	Type 1; FeLoBAL	0011 0001
083448.48+015921.1	128.702 02	1.989 21	2.594	21.19 ± 0.05	6.88 ± 0.09	14.31	–	214 ± 7	2864 ± 73	EREW, type 1	1000 0001
220337.79+121955.3	330.907 49	12.332 04	2.626	21.57 ± 0.05	7.45 ± 0.14	14.12	–	262 ± 3	1072 ± 10	EREW, type 2	1000 0010
085124.78+314855.7	132.853 29	31.815 48	2.638	21.63 ± 0.07	6.79 ± 0.08	14.84	–	76 ± 5	3584 ± 181	Type 1, $W1W2$ dropout	0100 0001
100424.88+122922.2	151.103 70	12.489 52	2.640	22.15 ± 0.12	7.87 ± 0.19	14.28	12.3	–	–	Tpye FeLoBAL	0011 0001
104611.50+024351.6	161.547 96	2.731 03	2.772	21.51 ± 0.07	7.11 ± 0.11	14.40	–	203 ± 7	5181 ± 144	Type 1, N v/Ly $\alpha > 1$, EREW	1000 0001
155434.17+110950.6	238.642 38	11.164 07	2.936	21.19 ± 0.05	6.63 ± 0.08	14.56	–	–	–	Type 1, BAL, probably FeLoBAL	0010 0001
135959.73+052512.3	209.998 88	5.420 08	3.055	22.08 ± 0.11	7.27 ± 0.09	14.81	–	70 ± 10	7250 ± 833	Type 1, $W1W2$ dropout	0100 0001
022052.11+013711.1	35.217 15	1.619 76	3.138	21.82 ± 0.08	7.08 ± 0.09	14.74	–	341 ± 19	2843 ± 167	EREW, Type 1, $W1W2$ dropout	0100 0001
101439.51+413830.6	153.664 66	41.641 83	4.360	21.84 ± 0.08	7.74 ± 0.16	14.10	–	118 ± 8	13568 ± 684	Type 1, (Fe)LoBAL	0010 0001

Table 3. The classifications of the optical spectra of the extremely red quasar sample, the bitwise value associated with each classification and the number in the sample. Aside from the type 1/type 2 dichotomy, the categories are not mutually exclusive. Quasars are flagged as 'radio detected' if they are detected in the FIRST survey.

General description	Bitwise value	Number in sample
Type 1 quasar	0000 0001	37
Type 2 quasar	0000 0010	28
Starburst	0000 0100	5
Post-starburst	0000 1000	2
Radio detected	0001 0000	37
(Fe)LoBAL	0010 0000	10
*W*1*W*2 dropouts	0100 0000	3
'Extreme' REWs	1000 0000	12

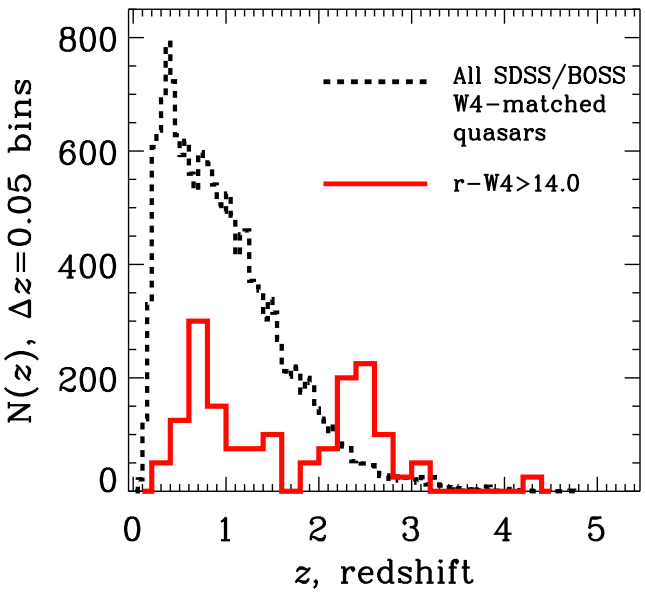

Figure 3. The redshift distribution of the 17 744 SDSS/BOSS quasars with good *W*4 matches is given by the black (dashed) histogram. The redshift distribution of extremely red quasars (with $r - W4 > 14$) is given by the solid (red) line. It has a binwidth of $\Delta z = 0.20$ and is renormalized to peak at 300. This maximum bin, at $z \approx 0.70$, actually has 12 objects.

filled circles. We also split the extremely red quasar sample into three broad classes, 'type 1' (Section 4.1), 'type 2' (Sections 4.2 and 4.3) and the EREW objects (Section 4.7).

Fig. 7 shows that the type 2 and EREW quasar populations are redder in (*W*2–*W*3) than the general *W*4-detected population. Upon visual inspection of the *W*4-detected objects with very red, $(W2 - W3) \gtrsim 3.8$ colours, many were found to lie along the ecliptic and did not have secure *W*4 photometry due to Mars, Jupiter and Saturn producing a significant number of spurious mid-IR detections.[4] These detections are not plotted in Fig. 7 and does not affect any of our $r - W4 > 14$ extremely red quasars.

In $(W1 - W2)$, the extremely red quasar population is perhaps slightly more representative of the *W*4-detected population; none of the red quasars are bluer than $(W1 - W2) \approx 0.5$. The *W*1*W*2*W*3 colour–colour diagram has become a key diagnostic for *WISE* objects, and its power in separating different classes of objects is seen in Wright et al. (2010); Eisenhardt et al. (2012) and Yan et al. (2013). In particular, Eisenhardt et al. (2012) use a colour selection based on *W*1*W*2*W*3 colours to select '*W*1*W*2 dropouts'. Three of our quasars satisfy this criterion, signified by the stars in Fig. 7. We discuss these objects in Section 4.6.

[4] wise2.ipac.caltech.edu/docs/release/allsky/expsup/sec5_3.html#planets

3.3 Radio properties

Table 2 also gives the radio fluxes of the $r_{\rm AB} - W4_{\rm Vega} > 14$ sample. 37 (56 per cent) of the full extremely red quasar sample is detected in the FIRST survey (Becker et al. 1995), which has a flux limit of ≈1 mJy at 20 cm, with 22 out of 28 objects at $z < 1.1$ (79 per cent) being detected. The magnitude of radio flux at 20 cm ranges from 0.55 to 960 mJy.

While the radio loudness is typically defined by the ratio of the 5 GHz radio to 4400 Å flux densities (e.g. Kellermann et al. 1989; Padovani et al. 2003), with the advent of the FIRST and SDSS surveys, much of the recent analysis of radio loudness has been done in terms of the 20cm to *i*-band ratio, $\mathcal{R} = f_{\rm radio}/f_{\rm optical}$, e.g. Ivezić et al. (2002), White et al. (2007) and Kratzer & Richards (2015). Typically no *k*-correction is applied as the mean spectral index in the radio and optical are similar (though this assumption may not hold true for these extremely red, and unusual objects). While there is no true gap in the distribution of $\mathcal{R}$, at $\mathcal{R} \sim 10$ there is a subtle change in the distribution (e.g. White et al. 2007; Kratzer & Richards 2015) and it is common to refer to objects with $\mathcal{R} \geq 10$ as 'radio loud'. The value of $\mathcal{R}$ can be calculated straight from Table 2 for each of our objects, and we find that all 37 of our radio-detected objects are nominally radio loud. However, without knowing the extent of reddening from dust in our sources, these values should be considered as an upper limit to the true value of $\mathcal{R}$. We also find that all of the 37 radio-detected objects are unresolved in FIRST.

A total of 30 objects (46 per cent) in our sample have a radio target selection flag set indicating that these objects were detected in the FIRST survey and passed the SDSS/BOSS quasar selection to be observed as quasar targets. Of these 30 objects, 10 are from SDSS and 20 from BOSS. 17 objects (26 per cent) are selected for spectroscopy *solely* due to their radio properties, all of which are from BOSS.

Yan et al. (2013) discovered ULIRGs at $z \sim 2$ with extremely red colours, which suggests that star formation will lead to an enhancement of the *W*4 emission we detect from our sample. While the sample definition of $r - W4 > 14$ selects quasars that are red due to dust obscuration (i.e. the targeted obscured quasar population), there is the possibility it will also select systems with particularly bright IR emission due to star formation. The large fraction of radio-detected quasars in the resulting sample, and the known relations between radio and IR emission from star formation, suggest that this may be an aspect of the extremely red quasar selection.

To investigate this further, we calculate rest-frame 1.4 GHz radio luminosity from the observed fluxes using a radio spectral index of $\alpha = -0.7$. In the first instance, we assume that all of the radio emission is due to star formation, which will result in upper limits on the SFR derived from the radio and MIR. We use the conversions between radio and star formation rates reported in Bell (2003) to calculate the necessary SFRs and total IR luminosity of star formation $L_{\rm SFR,\ 8-1000\,\mu m}$. Then we scale seven star formation templates from Kirkpatrick et al. (2012) and Mullaney et al. (2011) to match the SFRs necessary to explain the observed radio emission. We then redshift them to the redshift of the target, convolved with the *W*4 filter from Jarrett et al. (2011) and calculate the predicted IR flux.

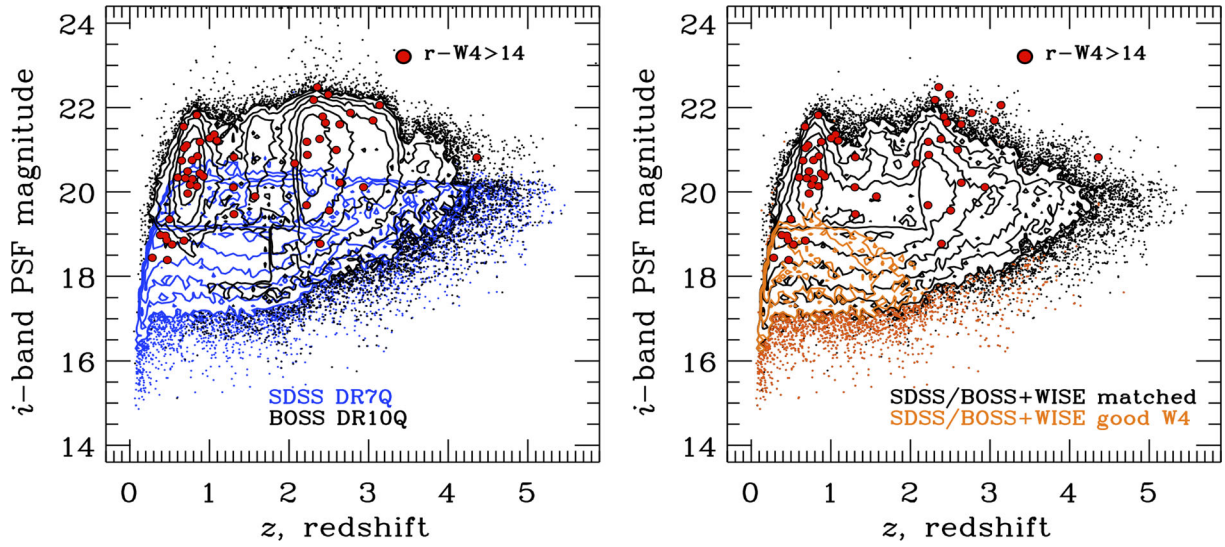

Figure 4. The redshift versus i −band magnitude distribution for the extremely red quasars satisfying the $r - W4 > 14$ selection. Left: the blue and black contours show the distributions for the SDSS DR7 and the BOSS DR10 quasar catalogues, respectively. Right: the black contours show the distribution of all SDSS/BOSS quasars that have a match in any of the *WISE* bands, while the orange contours are SDSS/BOSS quasars with good 22 μm *W4*-band detections.

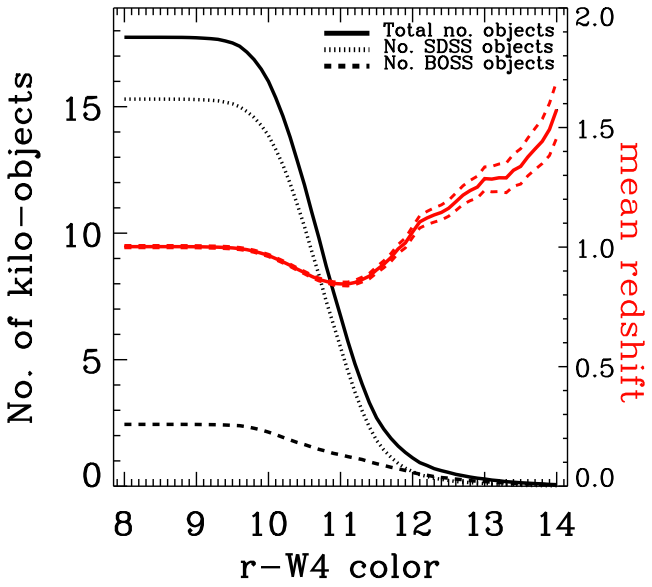

Figure 5. The number of quasars selected, and their mean redshift, as a function of $r_{AB} - W4_{Vega}$ colour. The dashed (red) lines give the 1σ spread on the mean redshift value. In total, 17 744 quasars have $r - W4 > 8.0$. Note that the extremely red quasar sample at $r - W4 \geq 14.0$ is the tail end of the *W4*-matched quasar sample.

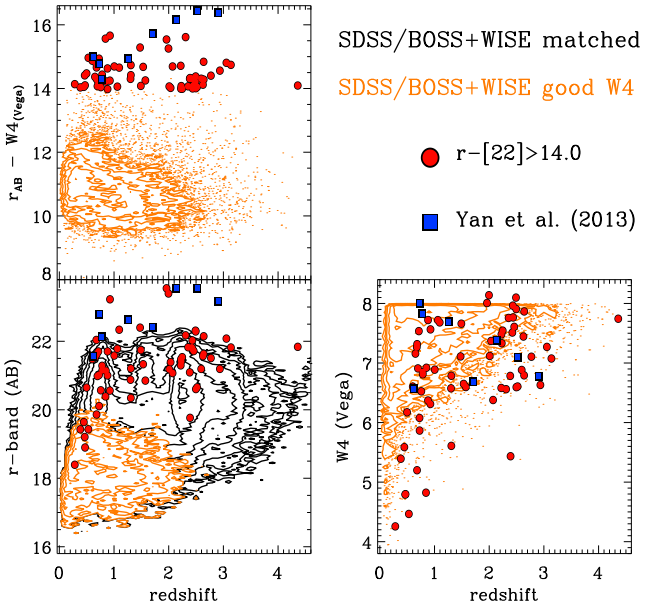

Figure 6. The magnitude–redshift and colour–redshift diagrams for the objects with a *WISE* detection (black contours) and objects with a good *W4* match (orange contours). The $r - W4 > 14$ extremely red quasar population is shown by the red circles. Top left: redshift versus *r*–*W4* colour; bottom left: redshift versus *r*-band AB magnitude and bottom right: redshift versus *W4* Vega magnitude. The data from Yan et al. (2013) are indicated by the blue squares.

Fig. 8 shows the ratio between the observed and the predicted *W4* fluxes; those are shown as black points, where the error bars reflect the spread amongst templates (and therefore provide a measure of the systematic error). For objects undetected in the radio, we can only calculate an upper limit on the SFR rate and thus a lower limit on the observed-to-predicted flux ratio; those are shown as red upward arrows, and those are conservative (i.e. the lowest lower limit of the seven templates). A ratio of >1 means the MIR emission is likely AGN dominated, while ratios <1 mean the predicted SFR is less than expected, given the radio flux.

There are 37 objects detected in the radio; if all the radio flux is associated with star formation, which is unlikely, then for these objects the median luminosity due to star formation would need to be $L_{8-1000\,\mu m} = 10^{13.6}\,L_{\odot}$ in order to explain the median radio luminosity of $\nu L_{\nu}[1.4\,\mathrm{GHz}] = 10^{41.6}$ erg sec^{-1}. In other words, these objects would need to be forming stars at the median rate of $\approx$7700 $M_{\odot}$ yr^{-1} in order to explain the observed radio emission, and this rate is ∼4–10× higher than the e.g. 850 μm-selected sub-millimetre galaxy (SMG) population at redshifts $z \sim 2$–3 (Fu et al. 2013; Wardlow et al. 2013; Casey, Narayanan & Cooray 2014). However, this SFR is an upper limit, as the AGN is almost certainly contributing significant flux in all objects. It is more likely that both

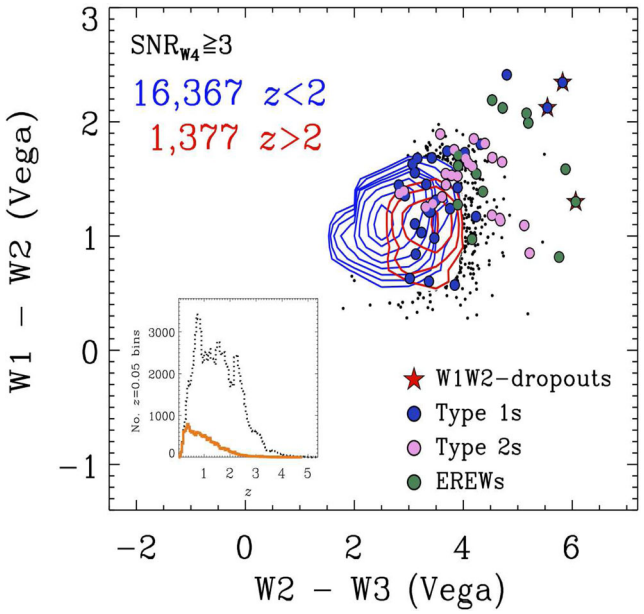

Figure 7. The mid-IR '*W*1*W*2*W*3' colour–colour distributions for objects in the SDSS and BOSS quasar catalogues, that have a match in *WISE* and have a *W*4-band SNR ≥ 3. Objects with redshifts $2 < z < 2$ are given by the blue and red contours, respectively, with the contouring level the same for the subsets of the distributions. The insert gives the redshift distribution for the *W*4-matched *WISE* sample which have good *W*1*W*2*W*3 detections (dashed histogram) and which pass the 'good *W*4' criteria (filled histogram). The large coloured points indicated the $r - W4 > 14$ quasars. We split this sample into three broad classes. The EREW sample generally lies on the edge of the overall *W*4-matched population, with roughly half the sample having very red colours i.e. $W2 - W3 \gtrsim 4.5$. The stars signify objects that pass the '*W*1*W*2 dropout' selection of Eisenhardt et al. (2012, see text for details).

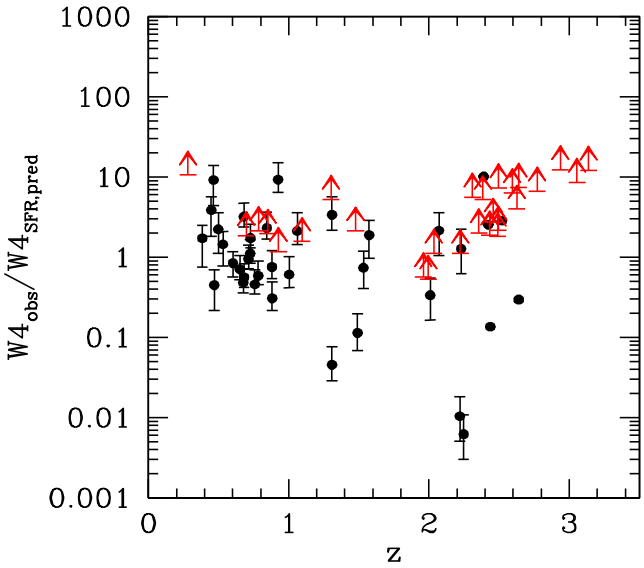

Figure 8. The ratio between the observed *W*4 flux of our sample and the *W*4 flux that would be expected given the observed radio luminosities and the conversions between radio and star formation rates reported in Bell (2003). A ratio of >1 means that the *W*4 emission is likely AGN dominated. For objects undetected in the radio (FIRST) survey, we only calculate an upper limit on the star formation rate and thus a lower limit on the observed-to-predicted flux ratio, given by the red arrows.

the radio emission and the *W*4 emission in these objects are due to the AGN and star formation, and thus the SFRs are more in line with those of SMGs and *WISE*-selected luminous IR galaxies (Wu et al. 2012; Jones et al. 2014, 2015; Tsai et al. 2015).

The two points with the lowest $W4_{obs}/W4_{SFR,\,predicted}$ ratios are potentially beamed sources with an apparent extremely high radio luminosity $\nu L_{\nu}[1.4\,\mathrm{GHz}] \simeq 10^{44.5}$ erg s^{-1} which has nothing to do with star formation in the host galaxy (though our data are insufficient to determine the origin of the *W*4 emission in these sources). For the less-extreme sources at $z < 1$, we find that the required median SFR necessary to explain the observed radio and *W*4 emission is 2180 M$_{\odot}$ yr^{-1}, which is still very high, but could potentially be the result of an e.g. (major) merger. While we do not have direct observations (e.g. far-IR) which would rule out such star formation rates, various authors find it unlikely that star formation dominates mid-IR and radio emission of luminous type 2 quasars at $z < 1$ (e.g. Harrison et al. 2014; Zakamska & Greene 2014; Zakamska et al., in preparation).

The remaining objects are undetected in the radio and therefore we can place only upper limits on star formation rates. For this population, we find the median lower limit $W4_{obs}/W4_{SFR,\,predicted}$ of 2.4, meaning that the star formation is inadequate by at least this factor in explaining the observed *W*4 flux. Thus we conclude that the *W*4 fluxes in these objects must be dominated by the AGN as well. However, it seems that ultimately, we currently do not have enough data to determine whether the radio emisson is due to AGN or star formation. New FIR/submm data is required, with further SED decomposition, and indeed this is where future analysis will be concentrated (Hamann et al., in preparation; Zakamska et al., in preparation).

4 CLASSIFICATIONS FROM OPTICAL SPECTROSCOPY

The spectra of the extremely red quasar sample are publicly available at the SDSS-III Science Archive Server.[5] We broadly classify the objects that satisfy the $r - W4 > 14$ selection into: (i) unobscured (but reddened) type 1 quasars possessing broad lines (bitwise value 1 in Table 3); (ii) objects that show evidence for being narrow-line type 2 quasars from their optical spectra (bitwise value 2 in Table 3); (iii) objects that suggest ongoing, or recently ceased star formation (bitwise values 4 and 8); (iv) radio-detected quasars (in the FIRST survey, bitwise value 16); (v) quasars with blueshifted absorption features (bitwise value 32); (vi) objects that are not detected in the *WISE* *W*1/2 bands (bitwise 64) and (vii) a class of type 1 sources with extreme REW in their UV broad lines, namely, REW>150 Å in either C IV or Mg II (bitwise 128). These classification groups are not mutually exclusive; several objects are assigned to multiple groups. However, we class all of the sources as either type 1 (37/65; 57 per cent) or type 2 (28/65; 43 per cent). These sources are indicated by the bitwise values in the last column of Table 2 and are described in Table 3. Example spectra are presented in what follows.

4.1 Type 1 quasars

Fig. 9 presents the spectra of six examples of extremely red quasars, classified as type 1 based on broad emission lines seen in their optical spectroscopy. Where measured, the mean line widths are FWHM(Mg II) ∼6440 km s^{-1} and FWHM(C IV) ∼4900 km s^{-1}.

[5] http://dr10.sdss3.org

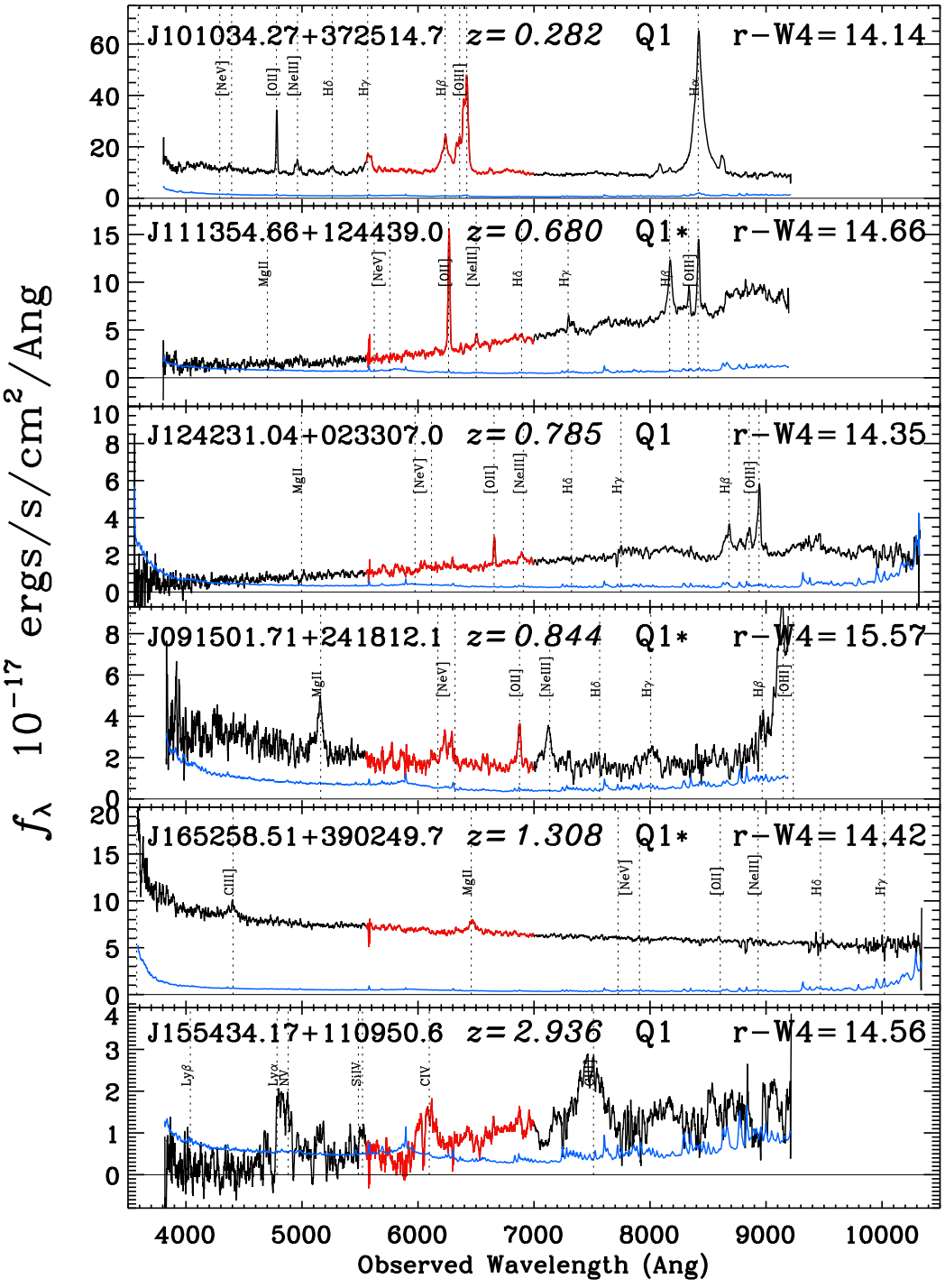

Figure 9. Examples of extremely red quasars classified as type 1 quasars based on their optical spectroscopy. The SDSS name, redshift, classification and $r - W4$ colour are given in each panel. The red part of the spectrum marks the contribution to the observed r-band flux, while the blue line is the estimated error per pixel (Lee et al. 2013). The spectra are smoothed using an 8 pixel boxcar average. Prominent emission lines often seen in AGN spectra; Ly β 1025.72, Ly α 1215.67, N v 1240.14, Si iv 1393.76, 1402.77, C iv 1548.19, 1550.76 C iii] 1908.73, Mg ii 2798.75 Ne v 3346.82, 3426.84 [O ii] 3728.48 [Ne iii] 3869.85, H δ 4102.89, H γ 4341.68, H α 4862.68, [O iii] 4960.30, 5008.24 and H α 6564.61 Å, are marked by the vertical dashed lines, where we use vacuum wavelengths for identifying emission lines. The feature at 5575 Å in the lower two panels is the [O i] bright sky line. Spectra that cut off at 3800 and 9200 Å are SDSS spectra, while BOSS spectra extend to 3600 and 10 400 Å. Objects with starred classifications were targeted due to their radio properties. Note that the y-axis scales are different in each panel.

Fig. 9 lists the SDSS name, redshift, classification (from Table 3) and $r - W4$ colour of each object.

The spectra in Fig. 9 are heterogeneous; some show blue continua, while some are red. The first object (with the lowest redshift in our sample) has unusually broad [O iii] with non-Gaussian structure (Liu et al. 2010, see also Section 4.4). Many of the examples of type 1 quasars from our selection appear to be significantly reddened (Richards et al. 2003) often with a host galaxy component.

Glikman et al. (2013) identify dust-reddened quasars by matching the FIRST radio catalogue to the UKIRT Infrared Deep Sky Survey (UKIDSS; Lawrence et al. 2007). This study identified 14 reddened quasars with $E(B-V) > 0.1$, including three at $z > 2$. However, Glikman et al. (2013) find no heavily reddened ($E(B-V) \gtrsim 0.5$) quasars at high redshifts ($z > 2$). The object ULASJ1234+0907 ($z = 2.503$) discovered by Banerji, Fabian & McMahon (2014) is currently the reddest broad-line type 1 quasar known, with $(i-K)_{\rm AB} > 7.1$. Since all our extremely red quasars have $i \lesssim 22$ mag and a range of $1.62 < (i-K)_{\rm AB} < 4.73$, none of our objects have optical-to-near IR colours as red as ULASJ1234+0907.

We note the object J165258+390249 has a relatively blue continuum and is clearly not suffering from dust obscuration. This object may be optically variable, and at the time of the optical and IR photometry had a large enough $r - W4$ to satisfy our colour cut. We also note it is a radio source, and has features consistent with an optical blazar spectrum. This further highlights the importance of understanding the radio properties (and potentially the synchrotron radiation contribution) of these quasars and how it affects the IR and the resulting sample of objects.

4.2 Type 2 quasar candidates at low redshift

We define type 2 quasars as objects with narrow permitted emission lines that do not have an underlying broad component, and with line ratios characteristic of non-stellar ionizing radiation (Zakamska et al. 2003; Reyes et al. 2008). Specifically, in type 2 quasars the broad-line region is completely blocked from the observer by strong obscuration ($A_V > 10$), and nuclear activity is inferred indirectly via the emission line ratios of ionized gas which are characteristic of photo-ionization by the quasar (Baldwin, Phillips & Terlevich 1981; Veilleux & Osterbrock 1987). At low redshifts, where Hβ and [O III] are accessible in the optical spectrum, we can define type 2 objects as those in which the kinematic structure of the permitted emission lines is similar to that of the forbidden lines; the permitted lines should not display an additional broad (FWHM $\gtrsim 2000$ km sec^{-1}) component. We also require [O III]/H$\beta > 3$.

Fig. 10 presents examples of type 2 quasar candidates at $z \lesssim 1$. No line-fitting has been performed, but all objects in this class are seen by visual inspection to have similar same kinematics in the permitted H β and forbidden [O III] lines. In the extremely red quasar sample, the quasar nature of the type 2 candidates is not in doubt: the typical values of [O III]/H β are 10 or greater, and high-ionization species such as [Ne V] are detected in most cases. However, Hβ can be weak and there may be broad components in some H α lines (Zakamska et al., in preparation) which are redshifted out of the BOSS wavelength coverage.

Just over half (60 per cent) of our type 2s are at $z < 1$. This is due to the fact that we are using the spectroscopic quasar catalogues as our initial sample, before matching to the *WISE* photometry. Thus, from the requirement of having a relatively bright detection in the optical (cf. the Brand et al. studies) there will be a selection bias towards lower redshift objects.

Among the 28 objects with $z < 1.1$, 20 (71 per cent) are classified as type 2 candidates from their optical spectra; see Fig. 10. This high fraction of type 2 objects is completely uncharacteristic of the parent sample of the SDSS/BOSS quasars, making it clear that the selection based on high IR-to-optical colours can indeed recover obscured quasars. All seven type 2 quasars in our sample that were observed before 2006 July are found in the catalogue of Reyes et al. (2008).

4.3 Type 2 quasar candidates at high redshift

We find objects that have narrow emission lines, weak continua and satisfy the definition of type 2 candidates, at high redshift ($z > 1.5$) as well; see Fig. 11. The classifications are performed by visual inspection of the optical spectra and all objects in this class with $z > 1.5$ have FWHM(C IV) $\lesssim 2000$ km s^{-1}.

These objects have similar optical spectra to those described in Yan et al. (2013) and Alexandroff et al. (2013), although there are no objects in common between our sample and that presented in Alexandroff et al. (2013). Those authors present a sample of 145 candidate type 2 quasars from BOSS at redshifts between 2 and 4.3, using data from DR9 (Ahn et al. 2012). These objects are characterized by weak continuum in the rest-frame UV with a typical continuum magnitude of $i \approx 22$ (i.e. $M_i(z = 2.5) \approx -25$) and strong lines of C IV and Lyα, with FWHM ≤ 2000 km s^{-1}. Typical ($\sim L^*$) galaxies are $\geq$1 magnitude fainter at these redshifts (Marchesini et al. 2007, 2012), suggesting host-galaxy light is not sufficient to explain the continuum luminosity and some level of AGN light is getting through/around the absorber.

The reddest quasar in Alexandroff et al. (2013) has $r - W4 = 13.30$. In general, our selection of type 2 candidates is not as strict as that of Alexandroff et al. (2013), and we find no overlap between the sample here and the DR9-based sample in Alexandroff et al. (2013). While this class of object shows only narrow emission lines in the rest-frame UV spectra, Greene et al. (2014) obtained near-IR spectroscopy for a subset of the Alexandroff et al. (2013) sample, demonstrating that the Hα emission line consistently requires a broad component. This result implies that the typical extinction in these objects is $A_V \lesssim$ a few, sufficient to block the rest-frame UV continuum and broad lines but not the rest-frame optical – consistent with the (relatively) bright continuum.

4.4 Objects with starburst and post-starburst signatures

Our sample includes quasars that have starburst or post-starburst signatures in their optical spectra. Examples are given in Fig. 12.

The [O II]/[O III] ratio can be used as a starburst indicator in AGN and galaxies (e.g. Kauffmann et al. 2003; Groves, Heckman & Kauffmann 2006). Objects from our sample are placed into the starburst class if they exhibit evidence of obvious [O II] emission (Kennicutt 1998; Kewley & Dopita 2002; Kewley, Geller & Jansen 2004; Ho 2005; Moustakas, Kennicutt & Tremonti 2006; Mostek et al. 2012), though we acknowledge that [O II] emission can also be associated with the narrow-line region of the AGN.

The post-starburst objects are objects which have either a Balmer break, and/or an obvious Balmer series, originating from an A-star population that is not dominated by blue light from OB-stellar populations. Quasars with post-starbursting signatures have been identified previously (e.g. Brotherton et al. 1999, 2002; Cales et al. 2013, 2014), and Matsuoka et al. (2015) derive physical properties from optical spectra while Wei et al. (2013) study the MIR spectral properties of post-starburst quasars.

Both post-starburst objects in our sample are at relatively low redshift, and not all the host galaxy light is likely to be captured by the 2 arcsec spectroscopic fibre. However, the quasar J112657.76+163912.0 (hereafter J1126+1639) has a pronounced Balmer break and we estimate that the fraction of e.g A-star host galaxy flux required is at least that of the AGN. J1126+1639 may have other optical objects within the *W4* beam, as we mentioned in Section 2.2. J1126+1639 appears to be at the centre of a group/small

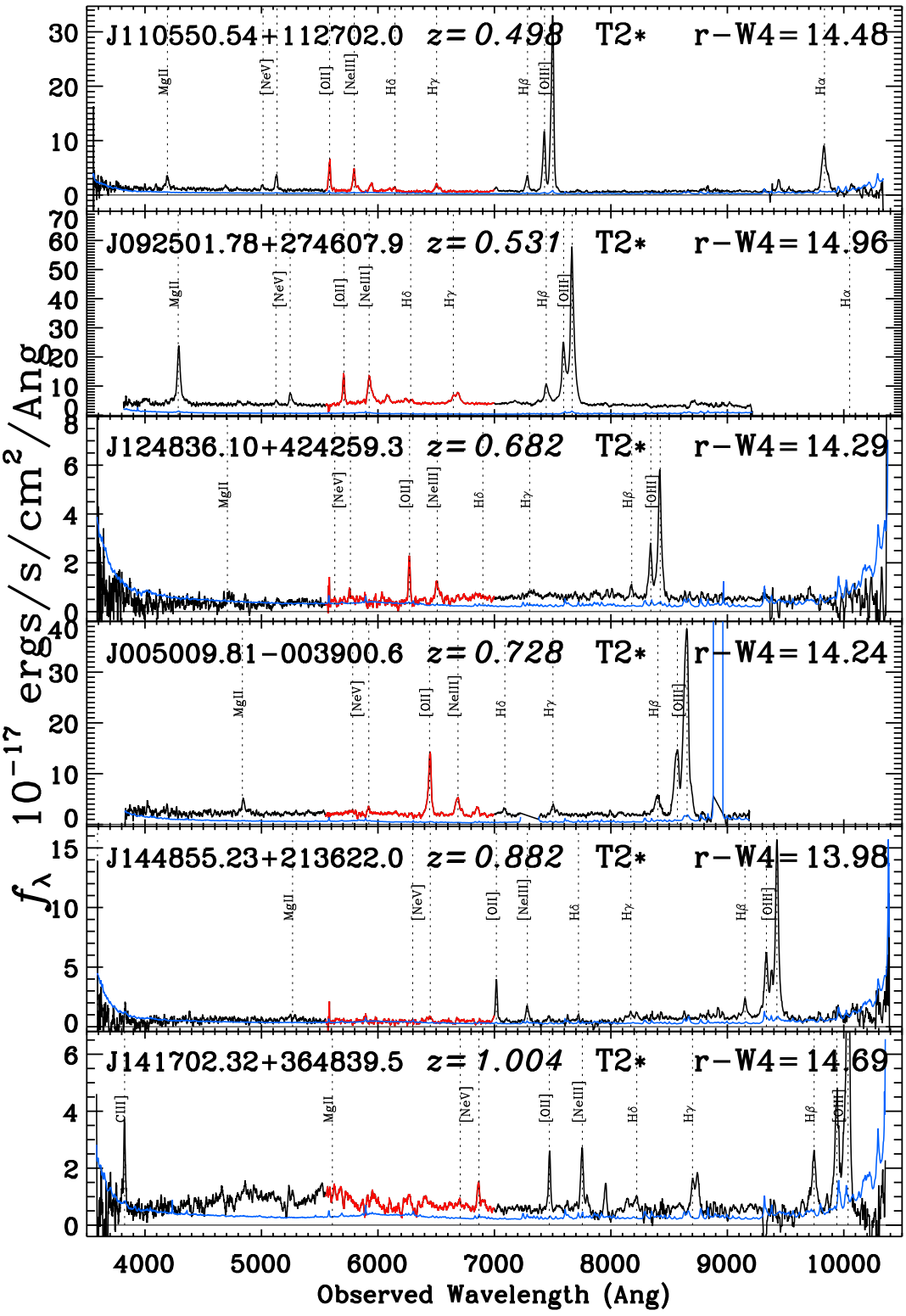

Figure 10. Same as for Fig. 9, except showing examples of extremely red quasars classified as type 2 quasars based on their optical spectroscopy, at $z \lesssim 1.1$.

cluster of other optically red galaxies. However, the other group members are *blue* in (*W*1–*W*2) colour, suggesting that these objects are not bright in *W*4. Our likely candidate appears disturbed in the SDSS optical image, suggesting that it hosts an ongoing merger.

4.5 BAL quasars

Our $r - W4 > 14$ quasar selection also finds broad absorption line (BAL) objects (Fig. 13). Although we do not use it for our classifications, the C IV balnicity index (BI; Weymann et al. 1991) for our extremely red BAL quasars as reported in the DR10Q

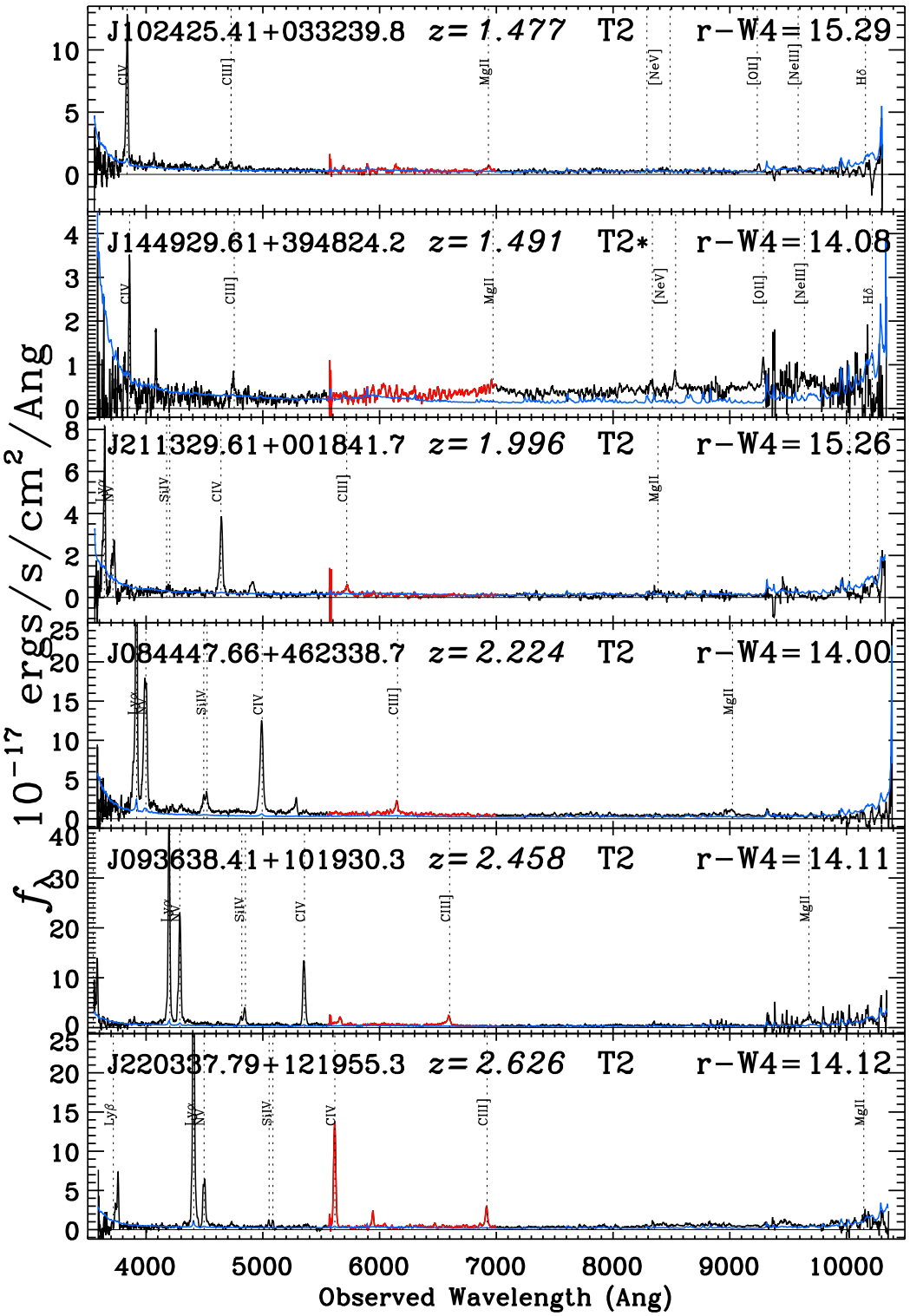

Figure 11. Same as for Fig. 9, except showing examples of extremely red quasars classified as type 2 quasars based on their optical spectroscopy, at $z \gtrsim 1.5$.

catalogue is generally $\log_{10}(\mathrm{BI_{C\,IV}}) \gtrsim 3$. In particular, we find examples of BALs that exhibit absorption from low-ionization species, i.e. LoBALs, and objects that have Fe II absorption, i.e. FeLoBALs. At $z = 4.36$, J101439.51+413830.6 is the highest redshift object in the full sample, but due to this high redshift, any Fe II absorption will be outside the optical wavelength coverage of the SDSS/BOSS spectra.

It has been known for some time that BALs can be redder (in optical-to-near IR colour) than the general quasar population e.g. Hall et al. (1997). Hall et al. (2002a) report on a number of heavily reddened, extreme BAL quasars discovered in SDSS, while Trump et al. (2006), Gibson et al. (2009) and Allen et al. (2011) explore this reddening–BAL relation. However, we note that the presence of the BAL objects in our sample is not due just to dust reddening; in these

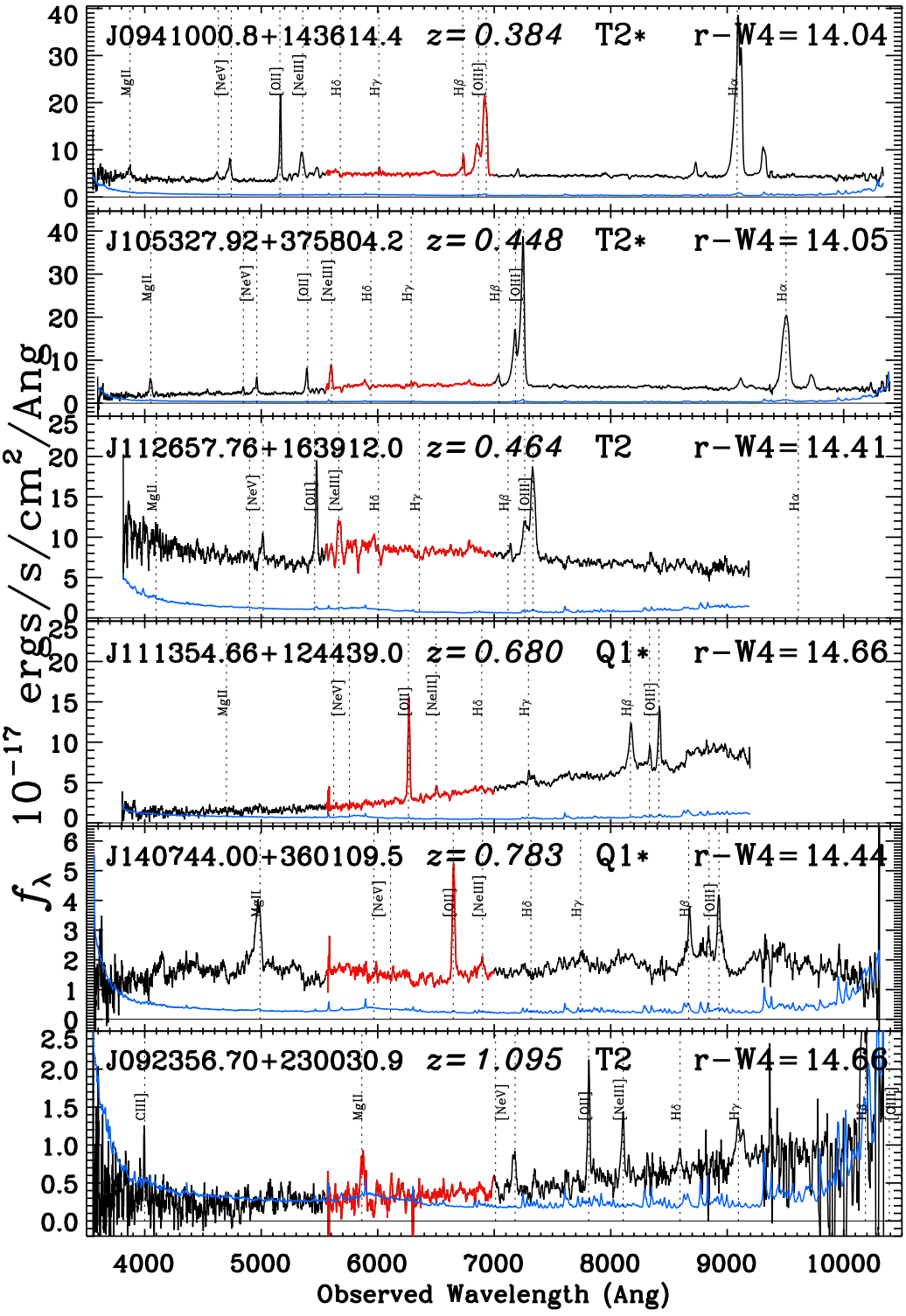

Figure 12. Same as for Fig. 9, except showing examples of extremely red quasars that display signatures of an ongoing, or post-, starbursting phase. In particular we identify the Balmer edge in J105327.92+375804.2 and J112657.76+163912.0.

objects, the BAL troughs remove a large fraction of the continuum that would otherwise contribute to the *r*-band flux, which makes the $r - W4$ colour even redder. We find FeLoBALs in our sample not because they have red continua, but because the BALs have wiped out the *r*-band flux; in this sense these are in the sample for different reasons than for the other very red quasars.

4.6 *W1W2* dropout quasars

Objects that are selected to be bright at 12 or 22 μm, but are undetected by *WISE* at 3.4 and 4.6 μm are '*W1W2* dropouts'. Eisenhardt et al. (2012) find ∼1000 such objects over the whole sky, including the $z = 2.452$ source *WISE* J181417.29+341224.9, a hyper-luminous IR galaxy (HyLIRG) with $L_{\rm IR} > 10^{13}\,{\rm L}_\odot$. *WISE*

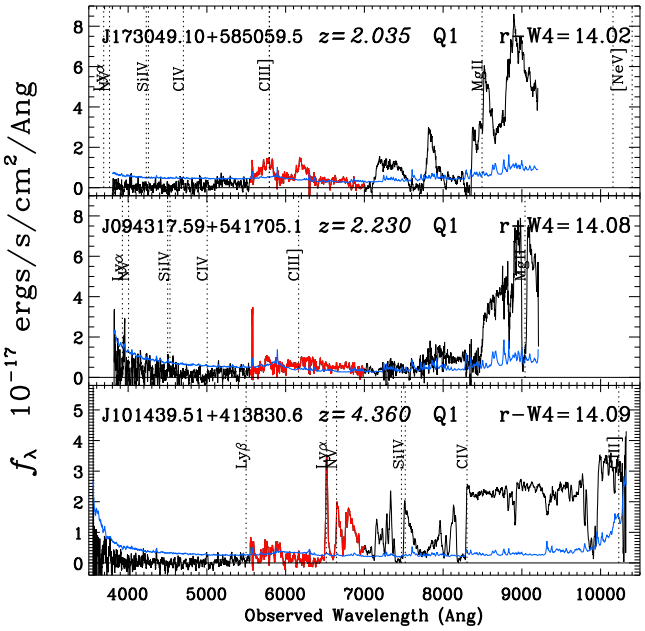

Figure 13. Same as for Fig. 9, except showing examples of the BAL quasars. These three objects are examples of the rare subclass of FeLoBALs. At $z = 4.36$, J101439.51+413830.6 is the highest redshift object in our full sample.

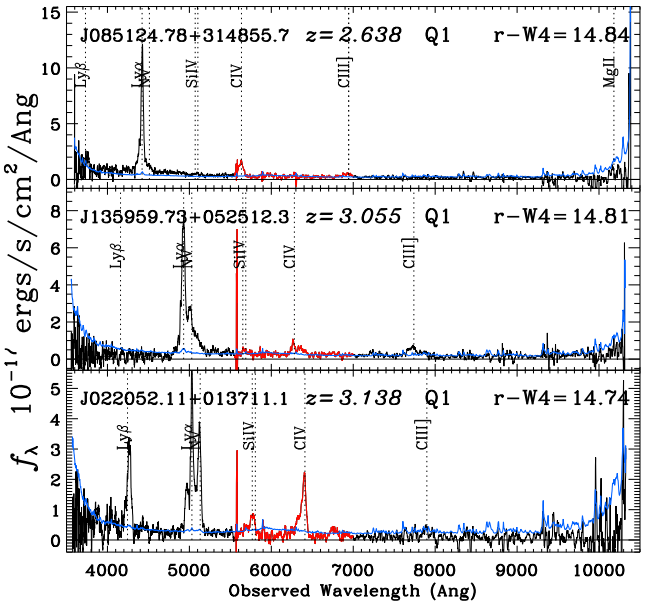

Figure 14. Same as for Fig. 9, except showing quasars that are '*W1W2* dropouts'. The feature at 5575 Å in the lower two panels is the [O I] bright sky line.

1814+3412 has a *W4* flux density of 14.38 ± 0.87 mJy; a 350 μm detection (Wu et al. 2012) implies a minimum bolometric luminosity of 3.7×10^{13} L$_\odot$ suggesting that the *W1W2* dropouts are extreme cases of luminous, hot (60–120 K) dust-obscured galaxies (Hot DOGs) possibly representing a short evolutionary phase during galaxy merging and evolution. Due to these dust temperatures, the *W1W2* dropouts are also known as 'Hot DOGs'.

Three of our 65 objects (∼5 per cent) satisfy the *W1W2* dropout selection criteria. Their optical spectra are shown in Fig. 14. These three quasars were all discovered by BOSS, have *r*-band fluxes of ≈5–8 μJy (cf. 2.25 ± 0.11 μJy for *WISE* 1814+3412) and redshifts $z = 2.638$–3.138, placing them in the HyLIRG regime.

4.7 Extreme EW objects

The objects that we present in Fig. 15 all have C IV FWHM > 2000 km s^{-1} (Table 2) and are thus classified as type 1 quasars. These six examples are a set of objects at $z \simeq 2$–3 which are characterized by EREWs of $\gtrsim$150 Å (the measured REWs from the C IV line are given in Fig. 15). Four sources have REW(C IV) > 200 Å. For comparison, typical quasars have REW(C IV) ≈ 25–50 Å. Some of the extreme REW sources also have unusual line properties, including high N V/Ly α, enhanced Si IV+O IV] and weak He II and C III]. Some also have strong Ly β and unusual Ly α profiles.

To quantify how unusual these objects are, we use emission-line data from the DR10Q catalogue to select sources that have: $2.0 < z < 3.4$, the visual inspection flag for BALs set to 0 (i.e. no BALs), FWHM(C IV) > 2000 km s^{-1}, and the ratio of the C IV REW to its uncertainty >3. A total of 98 807 quasars satisfy these criteria and in the cumulative distribution, 5.8 per cent of objects have REW(C IV) > 100 Å with 1.3 per cent having REW(C IV) > 150 Å. This is to be compared to 55 per cent (45 per cent) of the non-BAL type 1s with measurable C IV in our sample having REW(C IV) >100 (150) Å.

The quasar J1535+0903 (see Appendix A1) may also be a member of this class. We measure REW(C IV) = 136 Å, and REW(Mg II) ∼280 Å, the precise value depending on uncertain continuum placement. Like the N V/Ly α > 1 objects, J1535+0903 has very strong Al III λ1860.

The large REWs in these objects might be caused by suppressed continuum emission analogous to type 2 quasars in the unified model. However, the large line widths (at least compared to typical narrow-line regions; Liu et al. 2013) and in some cases very high electron densities (Section A1; Hamann et al., in preparation) suggest that the line-emitting regions are close to the central continuum source, as in typical broad-line regions. It therefore seems difficult to have dust obscuring the continuum source without also obscuring the broad emission lines. We investigate these issues further in Hamann et al. (in preparation).

5 COLOURS AND SELECTION OF THE EXTREMELY RED QUASARS

The optical SDSS/BOSS spectra of the extremely red quasars have been presented in Section 4. The heterogeneity of the optical spectra is immediately obvious. Upon visual inspection of the optical spectra, we have classified the extremely red quasar sample into various groups given in Tables 2 and 3. In this section, we explore the colours and selection of the extremely red quasars, in order to understand the relationship of the subclasses to each other, and with respect to the general quasar population.

5.1 Colours of the extremely red quasar groups

Fig. 16 presents the optical ($g - r$) colours for the full *W4* matched sample as a function of redshift. The mean ($g - r$) colour of all quasars with a *W4* detection is given by the blue line. As in Fig. 6, the three groups are indicated separately: type 1s (dark blue circles), type 2s (purple) and EREW objects (dark green). The extremely red quasars are generally redder than the mean *W4*-detected population in ($g - r$) colour. However, the EREW objects are the exception;

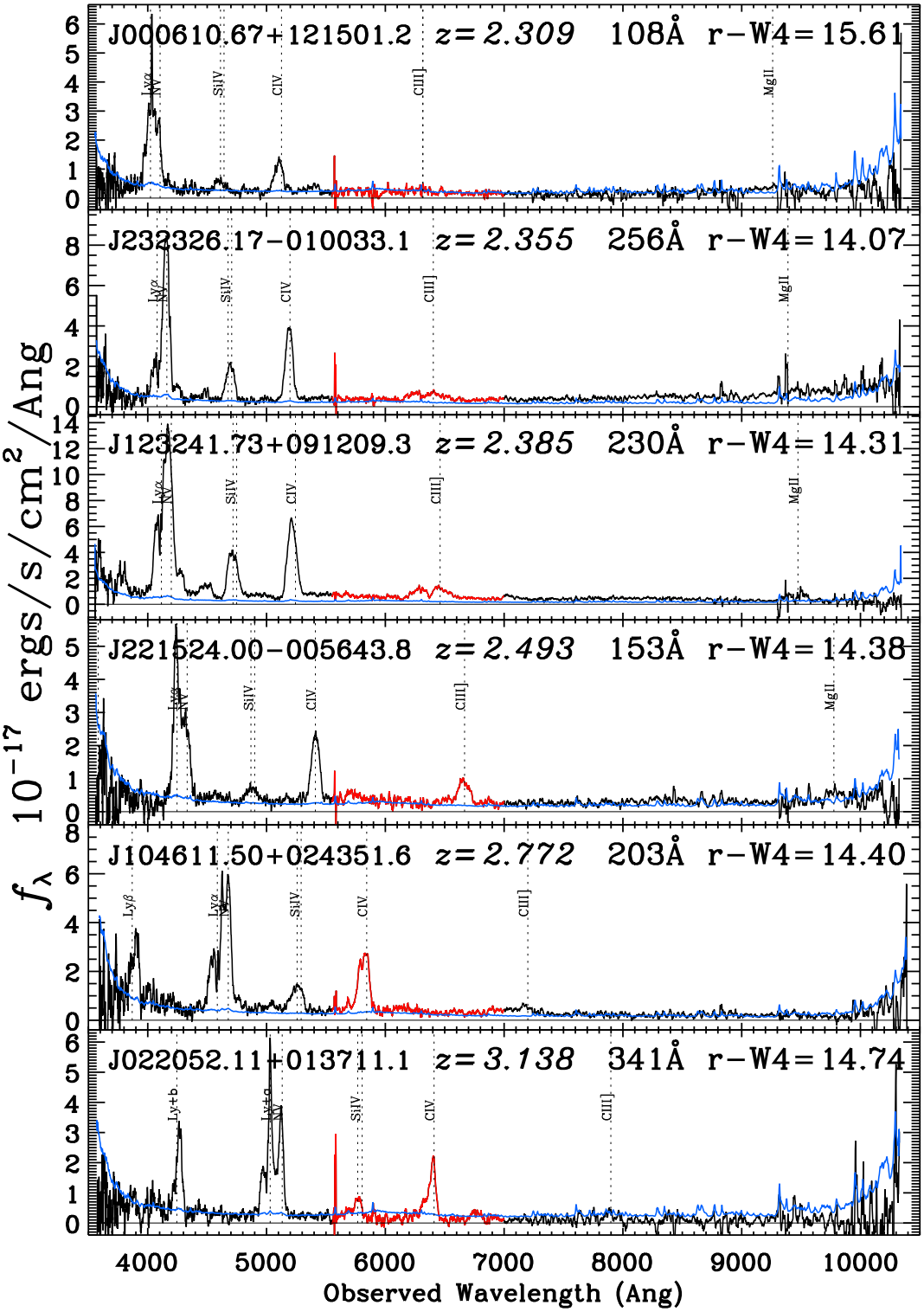

Figure 15. Same as for Fig. 9, except showing examples of the new set of 'EREW' objects. These objects possess large REWs of e.g. the C IV line (values given in Table 2), unusual profiles of the Ly α to N v complex (and the ratio of Ly α:N v) and flat continua in all examples. The quasar J022052.11+013711.1 (bottom panel) is also a *W*1*W*2 dropout (Fig. 14).

they *are bluer* than the full *W*4 population at all redshifts that they are found. This suggests that we are perhaps not sensitive to all EREWs, but just those objects with redshifts such that there are a number of very strong lines in the *g* band.

Fig. 17 presents the optical to IR colours, $(r - W1)$, $(r - W2)$, $(r - W3)$ and $(r - W4)$, for the full *W*4 matched sample as a function of redshift. The quasars detected at 22 μm generally have a $r - W1$ colour of 5 or more for redshifts $z = 0$–3, and again

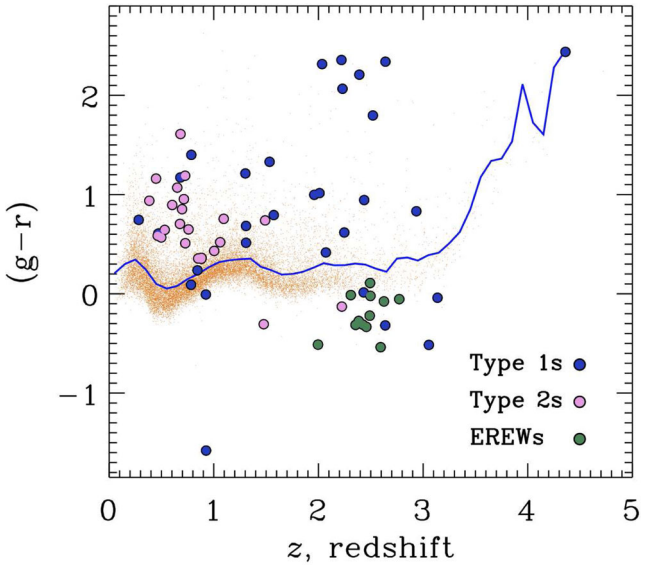

Figure 16. The optical ($g - r$) colour of the *W*4-matched quasars (orange points) as a function of redshift. The mean colour of the *W*4-matched sample is given by the solid blue line. At $z > 1.9$, the colour distribution of our extremely red quasars is impressively broad, demonstrating the heterogeneity of our sample. The EREW population is *bluer* than the overall population in ($g - r$) at $z \approx 2.5$. All optical magnitudes are AB.

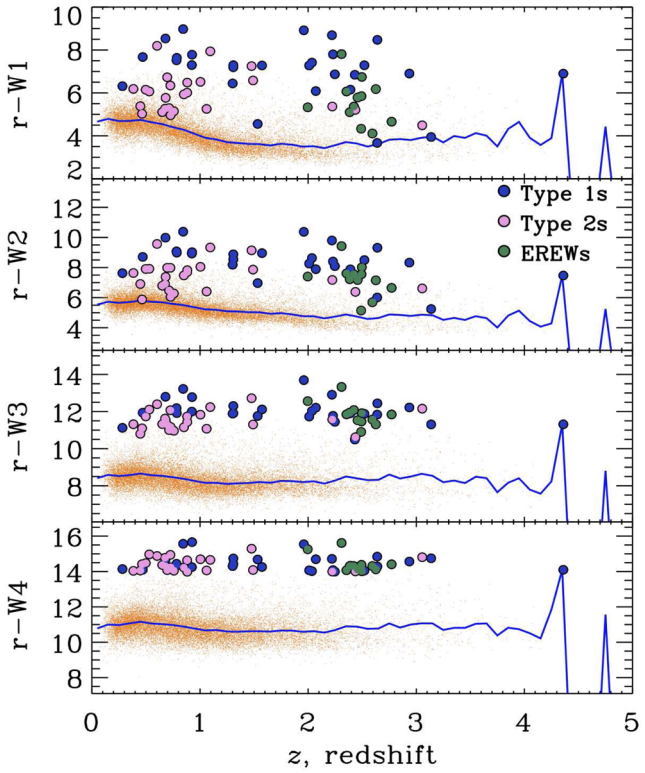

Figure 17. The optical–mid-IR colour for our *W*4-matched sample (orange points), with $r - W1$, $r - W2$, $r - W3$ and $r - W4$ shown from top to bottom. The mean colour of the *W*4-matched sample is given by the solid blue line. As the optical–MIR wavelength arm extends from *W*1 (3.4 μm) to *W*4 (22 μm) the selected population moves further away from the mean *W*4-matched sample. All optical magnitudes are AB, all *WISE* magnitudes are Vega.

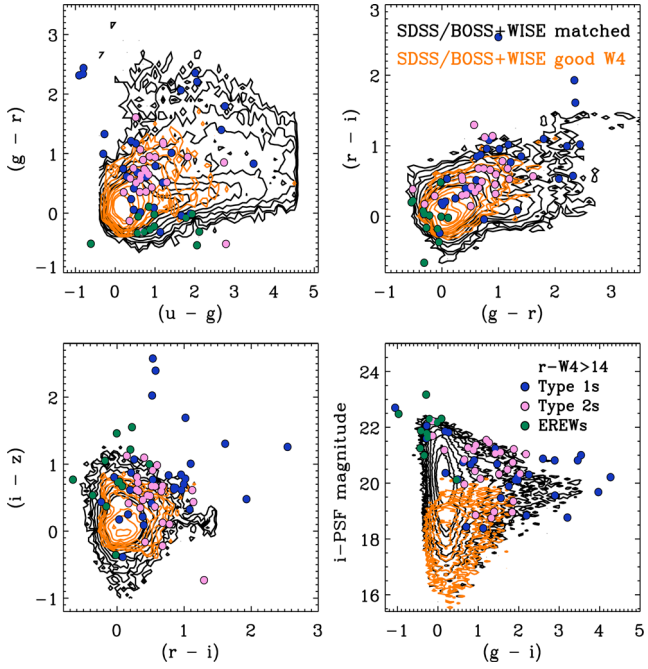

Figure 18. The optical colour–colour properties of SDSS/BOSS+*WISE* matched sample and the extremely red quasars: (top left): ($u - g$) versus ($g - r$); (top right): ($g - r$) versus ($r - i$); (bottom left): ($r - i$) versus ($i - z$); (bottom right): ($g - i$) versus *i*-band PSF magnitude. The distribution of all the SDSS/BOSS quasars with a good match in any *WISE* band is given by the black contours, while those objects with good *W*4 matches, and their colour distributions are given by the solid orange contours. We also show the location in colour–colour space of the three broad groups of our extremely red quasars – type 1s (dark blue circles), type 2s (purple) and EREW objects (dark green). The EREWs occupy a particular place in *gri*-colour–colour space, being very blue in ($g - i$) colour.

are redder than the general population of quasars. However, some of the type 2 objects do have ($r - W1$) and ($r - W2$) colours consistent with the general *W*4-detected population. However, all the extremely red quasars are considerably redder in ($r - W3$) which samples the ratio of rest-frame UV/blue to ∼6−7 μm light at redshift $z \sim 0.8$ and rest-frame far-UV to ∼3.4 μm colour at redshift $z \sim 2.5$. By design, our sample is much redder than the general *W*4-detected quasar population in ($r - W4$) colour, the latter of which has $10 \lesssim (r - W4) \lesssim 12$ for redshifts $z = 0$–3.

Fig. 18 shows the optical colour–colour distribution of the full SDSS/BOSS *WISE* matched sample (black contours), and those that have good *W*4 detections (orange contours). The extremely red quasar population tends to avoid the $(u - g) \leq 0.4$ and $(g - r) \leq 0.3$ region. The EREWs occupy a particular location in *gri* colour–colour and (*g*–*i*)–*i* colour–magnitude space. The EREWs have a very blue colour of $(g - i) \sim 0$, in contrast to the overall extremely red quasar population, which tend to have redder ($g - i$) colours than the general *W*4-matched sample. Further investigations into the colours and selection properties of the extremely red quasars and the EREWs are presented in Hamann et al. (in preparation).

Note that $z \approx 1.5$ is the redshift where C IV begins to contribute to the flux in the SDSS *g* band. Thus, type 2 quasars at $z \lesssim 1.5$ may have colours inconsistent with the SDSS/BOSS optical quasar selection criteria and thus enter the SDSS/BOSS sample via their radio properties. On the other hand, type 2 quasars at $z \gtrsim 1.5$ with C IV and Ly α emission really have blue continua.

6 SUMMARY AND CONCLUSIONS

We have matched the quasar catalogues of the SDSS and BOSS with *WISE* to identify quasars with extremely high IR-to-optical ratios $r_{\rm AB} - W4_{\rm Vega} > 14$ mag (i.e. $F_\nu(22\,\mu{\rm m})/F_\nu(r) \gtrsim 1000$). We identify 65 objects and note the following findings and conclusions.

(i) This sample spans a redshift range of $0.28 < z < 4.36$ and has a bimodal distribution, with peaks at $z \sim 0.8$ and $z \sim 2.5$.

(ii) We recover a wide range of quasar spectra in this selection. The majority of the objects have spectra of reddened type 1 quasars, type 2 quasars (both at low and high redshift) and objects with strong absorption features.

(iii) There is a relatively high fraction of type 2 objects at low redshift, suggesting that a high optical-to-IR colour can be an efficient selection of narrow-line quasars.

(iv) There are three objects that are detected in the *W*4 band but not *W*1 or *W*2 (i.e. '*W*1*W*2 dropout'), all of which are at $z > 2.6$.

(v) We identify an intriguing class of objects at $z \simeq 2$–3 which are characterized by equivalent widths of REW(C IV) $\gtrsim$ 150 Å. These objects often also have unusual line properties. We speculate that the large REWs may be caused by suppressed continuum emission analogous to type 2 quasars in the unified model. However, there is no obvious mechanism in the unified model to suppress the continuum without also suppressing the broad emission lines, thus potentially providing an interesting challenge to quasar models.

There are numerous avenues that the current data set can contribute to understanding quasar–host galaxy evolution and quasar orientation. Hamann et al. (in preparation) investigate the nature and origins of extreme broad emission line REWs in BOSS quasars. This will involve the detailed examination of emission-line properties for a subset of extreme REW quasars to gain a better understanding of the physical conditions and possible transient nature of this phenomenon. With the addition of ∼18 000 spectra of 22 μm detected quasars, one can significantly update Roseboom et al. (2013) where those authors investigate the range of covering factors, determined from the ratio of IR to UV/optical luminosity, seen in luminous type 1 quasars. However, the inhomogeneous selection of our data set makes computing the completeness challenging. One can also measure the clustering of the red-selected quasars, (e.g. DiPompeo et al. 2014; Donoso et al. 2014), using spectroscopic redshifts to enable a more robust 3D-clustering measurement. These investigations into environmental, and host galaxy, e.g. morphology, star formation, properties of the very red optical–IR colour-selected population will be able to elucidate on the nature of the 'extremely red quasar' population.

ACKNOWLEDGEMENTS

We thank R. M. Cutri and the IPAC team for the Explanatory Supplement to the *WISE* All-Sky and AllWISE Data Release Products resource. Peregrine McGehee and the IRSA HelpDesk were also very useful. NPR thanks Nathan Bourne for useful discussions on IR-to-radio flux ratios. AllWISE makes use of data from *WISE*, which is a joint project of the University of California, Los Angeles, and the Jet Propulsion Laboratory/California Institute of Technology, and NEOWISE, which is a project of the Jet Propulsion Laboratory/California Institute of Technology. *WISE* and NEOWISE are funded by the National Aeronautics and Space Administration. NPR acknowledges that funding for part of this project was supplied by NASA and the *Hubble* grant number: HST-GO-13014.06. FH acknowledges support from the USA National Science Foundation grant AST-1009628.

Funding for SDSS-III has been provided by the Alfred P. Sloan Foundation, the Participating Institutions, the National Science Foundation, and the U.S. Department of Energy. The SDSS-III web site is http://www.sdss3.org/. SDSS-III is managed by the Astrophysical Research Consortium for the Participating Institutions of the SDSS-III Collaboration including the University of Arizona, the Brazilian Participation Group, Brookhaven National Laboratory, University of Cambridge, University of Florida, the French Participation Group, the German Participation Group, the Instituto de Astrofisica de Canarias, the Michigan State/Notre Dame/JINA Participation Group, Johns Hopkins University, Lawrence Berkeley National Laboratory, Max Planck Institute for Astrophysics, New Mexico State University, New York University, Ohio State University, Pennsylvania State University, University of Portsmouth, Princeton University, the Spanish Participation Group, University of Tokyo, University of Utah, Vanderbilt University, University of Virginia, University of Washington and Yale University.

Facilities: SDSS, *WISE*

REFERENCES

Abazajian K. N. et al., 2009, ApJS, 182, 543
Adelman-McCarthy J. K. et al., 2006, ApJS, 162, 38
Ahn C. P. et al., 2012, ApJS, 203, 21
Ahn C. P. et al., 2014, ApJS, 211, 17
Alam S. et al., 2015, ApJS, 219, 12
Alexandroff R. et al., 2013, MNRAS, 435, 3306
Allen J. T., Hewett P. C., Maddox N., Richards G. T., Belokurov V., 2011, MNRAS, 410, 860
Antonucci R., 1993, ARA&A, 31, 473
Antonucci R. R. J., Miller J. S., 1985, ApJ, 297, 621
Assef R. J. et al., 2013, ApJ, 772, 26
Baldwin J. A., Phillips M. M., Terlevich R., 1981, PASP, 93, 5
Baldwin J. A. et al., 1996, ApJ, 461, 664
Baldwin J. A., Ferland G. J., Korista K. T., Hamann F., LaCluyzé A., 2004, ApJ, 615, 610
Banerji M., McMahon R. G., Hewett P. C., Gonzalez-Solares E., Koposov S. E., 2013, MNRAS, 429, L55
Banerji M., Fabian A. C., McMahon R. G., 2014, MNRAS, 439, L51
Becker R. H., White R. L., Helfand D. J., 1995, ApJ, 450, 559
Bell E. F., 2003, ApJ, 586, 794
Bolton A. S. et al., 2012, AJ, 144, 144
Brand K. et al., 2006, ApJ, 644, 143
Brand K. et al., 2007, ApJ, 663, 204
Brand K. et al., 2008, ApJ, 680, 119
Brandt W. N., Hasinger G., 2005, ARA&A, 43, 827
Brotherton M. S. et al., 1999, ApJ, 520, L87
Brotherton M. S., Grabelsky M., Canalizo G., van Breugel W., Filippenko A. V., Croom S., Boyle B., Shanks T., 2002, PASP, 114, 593
Bussmann R. S. et al., 2009a, ApJ, 693, 750
Bussmann R. S. et al., 2009b, ApJ, 705, 184
Cales S. L. et al., 2013, ApJ, 762, 90
Cales S., Brotherton M. S., Shang Z., Bennert V., Canalizo G., Diamond-Stanic A. M., 2014, American Astronomical Society Abstracts, Vol. 223, The Role AGN Play in the Evolution of Quasars Host Galaxies with Spectral Signatures of Post-Starburst Stellar Polulations. Am. Astron. Soc., Washington, DC, p. 115.06
Casey C. M., Narayanan D., Cooray A., 2014, Phys. Rep., 541, 45
Chiu K., Richards G. T., Hewett P. C., Maddox N., 2007, MNRAS, 375, 1180
Cutri R. M. et al., 2011, Technical Report, Explanatory Supplement to the WISE Preliminary Data Release Products, IPAC/Caltech
Dawson K. et al., 2013, AJ, 145, 10

Dey A. et al., 2008, ApJ, 677, 943
Diamond-Stanic A. M., Rieke G. H., 2010, ApJ, 724, 140
DiPompeo M. A., Myers A. D., Hickox R. C., Geach J. E., Hainline K. N., 2014, MNRAS, 442, 3443
Donley J. L. et al., 2012, ApJ, 748, 142
Donoso E., Yan L., Stern D., Assef R. J., 2014, ApJ, 789, 44
Draine B. T., Li A., 2007, ApJ, 657, 810
Eisenhardt P. R. M. et al., 2012, ApJ, 755, 173
Eisenstein D. J. et al., 2011, AJ, 142, 72
Elitzur M., 2008, New Astron. Rev., 52, 274
Elvis M., 2010, in Peterson B., Somerville R., Storchi-Bergmann T., eds, Proc. IAU Symp. 267, Co-Evolution of Central Black Holes and Galaxies. Cambridge Univ. Press, Cambridge, p. 55
Elvis M. et al., 1994, ApJS, 95, 1
Fu H. et al., 2013, Nature, 498, 338
Fukugita M., Ichikawa T., Gunn J. E., Doi M., Shimasaku K., Schneider D. P., 1996, AJ, 111, 1748
Fynbo J. P. U., Krogager J.-K., Venemans B., Noterdaeme P., Vestergaard M., Møller P., Ledoux C., Geier S., 2013, ApJS, 204, 6
Gibson R. R. et al., 2009, ApJ, 692, 758
Glikman E., Gregg M. D., Lacy M., Helfand D. J., Becker R. H., White R. L., 2004, ApJ, 607, 60
Glikman E., Helfand D. J., White R. L., Becker R. H., Gregg M. D., Lacy M., 2007, ApJ, 667, 673
Glikman E. et al., 2012, ApJ, 757, 51
Glikman E. et al., 2013, ApJ, 778, 127
Gordon K. D., Clayton G. C., 1998, ApJ, 500, 816
Greene J. E. et al., 2014, ApJ, 788, 91
Gregg M. D., Lacy M., White R. L., Glikman E., Helfand D., Becker R. H., Brotherton M. S., 2002, ApJ, 564, 133
Groves B. A., Heckman T. M., Kauffmann G., 2006, MNRAS, 371, 1559
Gunn J. E. et al., 1998, AJ, 116, 3040
Gunn J. E. et al., 2006, AJ, 131, 2332
Hall P. B., Martini P., Depoy D. L., Gatley I., 1997, ApJ, 484, L17
Hall P. B. et al., 2002a, ApJS, 141, 267
Hall P. B., Richards G T., York D. G., Keeton C. R., Bowen D. V., Schneider D. P., Schlegel D. J., Brinkmann J., 2002b, ApJ, 575, L51
Harrison C. M., Alexander D. M., Mullaney J. R., Swinbank A. M., 2014, MNRAS, 441, 3306
Ho L. C., 2005, ApJ, 629, 680
Hopkins P. F., Hernquist L., Cox T. J., Di Matteo T., Martini P., Robertson B., Springel V., 2005, ApJ, 630, 705
Hopkins P. F., Hernquist L., Cox T. J., Di Matteo T., Martini P., Robertson B., Springel V., 2006, ApJS, 163, 1
Ivezić Ž. et al., 2002, AJ, 124, 2364
Jarrett T. H. et al., 2011, ApJ, 735, 112
Jones S. F. et al., 2014, MNRAS, 443, 146
Jones S. F. et al., 2015, MNRAS, 448, 3325
Jurek R. J., Drinkwater M. J., Francis P. J., Pimbblet K. A., 2008, MNRAS, 383, 673
Kauffmann G. et al., 2003, MNRAS, 346, 1055
Keeton C. R., 2001, preprint (astro-ph/0102340v1)
Keeton C. R., Winn J. N., 2003, ApJ, 590, 39
Kellermann K. I., Sramek R., Schmidt M., Shaffer D. B., Green R., 1989, AJ, 98, 1195
Kennicutt R. C., Jr, 1998, ARA&A, 36, 189
Kewley L. J., Dopita M. A., 2002, ApJS, 142, 35
Kewley L. J., Geller M. J., Jansen R. A., 2004, AJ, 127, 2002
Khachikian E. Y., Weedman D. W., 1974, ApJ, 192, 581
Kirkpatrick J. D. et al., 2011, ApJS, 197, 19
Kirkpatrick A. et al., 2012, ApJ, 759, 139
Kocevski D. D. et al., 2012, ApJ, 744, 148
Kratzer R. M., Richards G. T., 2015, AJ, 149, 61
Krawczyk C. M., Richards G. T., Mehta S. S., Vogeley M. S., Gallagher S. C., Leighly K. M., Ross N. P., Schneider D. P., 2013, ApJS, 206, 4
Krawczyk C. M., Richards G. T., Mehta S. S., Vogeley M. S., Gallagher S. C., Leighly K. M., Ross N. P., Schneider D. P., 2015, ApJS, 999, 4
Lacy M. et al., 2004, ApJS, 154, 166
Lawrence A. et al., 2007, MNRAS, 379, 1599
Lee K.-G. et al., 2013, AJ, 145, 69
Liu X., Shen Y., Strauss M. A., Greene J. E., 2010, ApJ, 708, 427
Liu G., Zakamska N. L., Greene J. E., Nesvadba N. P. H., Liu X., 2013, MNRAS, 436, 2576
Maddox N., Hewett P. C., Warren S. J., Croom S. M., 2008, MNRAS, 386, 1605
Maddox N., Hewett P. C., Péroux C., Nestor D. B., Wisotzki L., 2012, MNRAS, 424, 2876
Mainzer A. et al., 2011, ApJ, 731, 55
Marchesini D. et al., 2007, ApJ, 656, 42
Marchesini D., Stefanon M., Brammer G. B., Whitaker K. E., 2012, ApJ, 748, 126
Martínez-Sansigre A., Rawlings S., Lacy M., Fadda D., Jarvis M. J., Marleau F. R., Simpson C., Willott C. J., 2006, MNRAS, 370, 1479
Matsuoka Y. et al., 2015, preprint (arXiv:1506.07535v3)
Melbourne J. et al., 2009, AJ, 137, 4854
Melbourne J. et al., 2012, AJ, 143, 125
Mostek N., Coil A. L., Moustakas J., Salim S., Weiner B. J., 2012, ApJ, 746, 124
Moustakas J., Kennicutt R. C., Jr, Tremonti C. A., 2006, ApJ, 642, 775
Mullaney J. R., Alexander D. M., Goulding A. D., Hickox R. C., 2011, MNRAS, 414, 1082
Nakos T. et al., 2009, A&A, 494, 579
Norman C. et al., 2002, ApJ, 571, 218
Oke J. B., Gunn J. E., 1983, ApJ, 266, 713
Padovani P., Perlman E. S., Landt H., Giommi P., Perri M., 2003, ApJ, 588, 128
Pâris I. et al., 2014, A&A, 563, A54
Peth M. A., Ross N. P., Schneider D. P., 2011, AJ, 141, 105
Polletta A., Weedman D., Hönig S., Lonsdale C. J., Smith H. E., Houck J., 2008, ApJ, 675, 960
Pope A. et al., 2008, ApJ, 689, 127
Reyes R. et al., 2008, AJ, 136, 2373
Richards G. T. et al., 2002, AJ, 123, 2945
Richards G. T. et al., 2003, AJ, 126, 1131
Richards G. T. et al., 2006, ApJS, 166, 470
Richards G. T. et al., 2009, AJ, 137, 3884
Rosario D. J. et al., 2015, A&A, 573, A85
Roseboom I. G., Lawrence A., Elvis M., Petty S., Shen Y., Hao H., 2013, MNRAS, 429, 1494
Ross N. P. et al., 2012, ApJS, 199, 3
Sanders D. B., Soifer B. T., Elias J. H., Madore B. F., Matthews K., Neugebauer G., Scoville N. Z., 1988, ApJ, 325, 74
Schlegel D. J., Finkbeiner D. P., Davis M., 1998, ApJ, 500, 525
Schneider D. P. et al., 2010, AJ, 139, 2360
Shen Y. et al., 2011, ApJS, 194, 45
Smee S. A. et al., 2013, AJ, 146, 32
Smith J. A. et al., 2002, AJ, 123, 2121
Soifer B. T., Helou G., Werner M., 2008, ARA&A, 46, 201
Souchay J. et al., 2009, A&A, 494, 799
Stern D. et al., 2002, ApJ, 568, 71
Stern D. et al., 2005, ApJ, 631, 163
Stern D. et al., 2012, ApJ, 753, 30
Stoughton C. et al., 2002, AJ, 123, 485
Trump J. R. et al., 2006, ApJS, 165, 1
Tsai C.-W. et al., 2015, ApJ, 805, 90
Urrutia T., Lacy M., Becker R. H., 2008, ApJ, 674, 80
Vanden Berk D. E. et al., 2001, AJ, 122, 549
Vardanyan V., Weedman D., Sargsyan L., 2014, ApJ, 790, 88
Veilleux S., Osterbrock D. E., 1987, ApJS, 63, 295
Veilleux S. et al., 2013, ApJ, 764, 15
Villforth C. et al., 2014, MNRAS, 439, 3342
Wardlow J. L. et al., 2013, ApJ, 762, 59
Wei P., Shang Z., Brotherton M. S., Cales S. L., Hines D. C., Dale D. A., Ganguly R., Canalizo G., 2013, ApJ, 772, 28
Weingartner J. C., Draine B. T., 2001, ApJ, 548, 296
Weymann R. J., Morris S. L., Foltz C. B., Hewett P. C., 1991, ApJ, 373, 23

White R. L., Helfand D. J., Becker R. H., Glikman E., de Vries W., 2007, ApJ, 654, 99
White M., Zheng Z., Brown M. J. I., Dey A., Jannuzi B. T., 2007, ApJ, 655, L69
Winn J. N., Lovell J. E. J., Chen H.-W., Fletcher A. B., Hewitt J. N., Patnaik A. R., Schechter P. L., 2002, ApJ, 564, 143
Winn J. N., Kochanek C. S., Keeton C. R., Lovell J. E. J., 2003, ApJ, 590, 26
Wright E. L. et al., 2010, AJ, 140, 1868
Wu X., Jia Z., 2010, MNRAS, 406, 1583
Wu J. et al., 2012, ApJ, 756, 96
Wu X.-B., Wang R., Schmidt K. B., Bian F., Jiang L., Fan X., 2011, AJ, 142, 78
Wu X.-B., Zuo W., Yang J., Yang Q., Wang F., 2013, AJ, 146, 100
Yan L. et al., 2013, AJ, 145, 55
York D. G. et al., 2000, AJ, 120, 1579
Zakamska N. L., Greene J. E., 2014, MNRAS, 442, 784
Zakamska N. L. et al., 2003, AJ, 126, 2125
Zakamska N. L. et al., 2005, AJ, 129, 1212
Zakamska N. L. et al., 2006, AJ, 132, 1496

APPENDIX A: NOTES ON INDIVIDUAL OBJECTS

A1 J153542.41+090341.1

Fig. A1 displays the spectrum of SDSS J153542.41+090341.1, hereafter J1535+0903, a remarkable object with a unique pattern of emission lines. We classify this quasar as a type 2 candidate based on line widths in both C IV (Table 2) and Mg II (FWHM $= 1600 \pm 60\,\mathrm{km\,s^{-1}}$). However, the exceptionally strong emission in Al III 1860 and in Fe II at ∼2300–2770 Å point to high densities indicative of a broad-line region and thus a type 1 classification. In particular, photoionization models by Baldwin et al. (1996) demonstrate that large ratios of Al III 1860 compared to the intercombination lines with similar ionizations, C III] 1909 and especially Si III] 1892, require densities $n_e \gtrsim 10^{12}$ cm^{-3}. Similarly, Baldwin et al. (2004) showed that this peculiar pattern of Fe II emission lines, dominated by a few spikes that include the resonance multiplets UV1 and UV 2,3, also requires densities $\gtrsim 10^{12}$ cm^{-3} in a gas with very low ionization parameter. Hamann et al. (in preparation) discuss this object further.

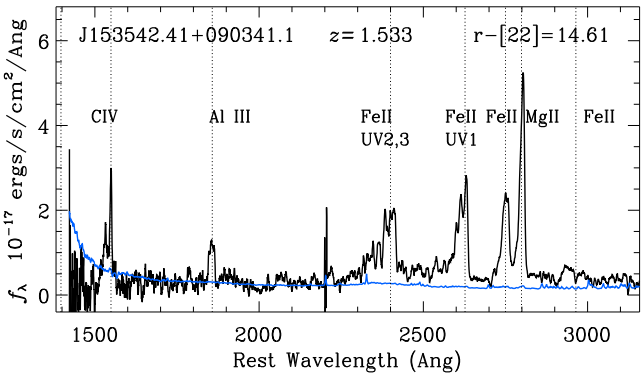

Figure A1. The spectrum of SDSS J153542.41+090341.1. This object has exceptionally strong Fe II emission in the UV1 (2600 Å), UV2/3 (2400 Å) and 2740 Å complexes with weak emission from other Fe II features.

A2 J013435.66-093102.9

SDSS J013435.66-093102.9, hereafter J0134-0931, is a gravitational lens. J0134-0931 has $r_{psf} = 21.33$, $W4 = 6.59$ and a redshift $z = 2.22$ and is also detected in FIRST at 0.96 Jy (integrated flux). J013435 has previously been reported and studied in detail in Gregg et al. (2002); Hall et al. (2002b); Keeton (2001); Keeton & Winn (2003); Winn et al. (2002) and Winn et al. (2003).

The flux is the linear sum of the lensing galaxy and the (boosted) quasar and at least one of the galaxy or quasar is exceedingly red. If there is dust in the foreground galaxy, it will extinct the quasar, and cause the r–$W4$ colour to be red. However, the foreground galaxy, at $z = 0.76$, is faint enough to not contribute significantly to the overall flux, so the background quasar is extremely red on its own.

This paper has been typeset from a TEX/LATEX file prepared by the author.